XFEL.EU TN-2012-002-01

TECHNICAL NOTE

X-Ray Photon Temporal Diagnostics for the European XFEL

Technical Review

November 2012

Bin Li

for the X-Ray Photon Diagnostics Group (WP74) at the European XFEL

European X-Ray Free-Electron Laser Facility GmbH

Albert-Einstein-Ring 19

22761 Hamburg

Germany

Contents

1 Introduction

With the commissioning of European X-ray Free Electron Laser (XFEL.EU) in 2015, it will enable the frontier research projects within the scope of Europe to investigate the extremely-small structures (Angstrom length scale) and the ultrafast phenomena & dynamics (sub-10-femtosecond time scale) at the same time [1]. The X-ray photon properties e.g. the pulse length and longitudinal profiles are particularly concerned by the experimental users in order to accurately characterize their measurements, to understand the phenomena and dynamics they investigated. The X-ray 'Pump-and-Probe' measurement is such a typical technique to investigate the ultrafast dynamics within the extremely small length scale, where the X-ray Free-Electron-Laser (XFEL) photon pulses are combined and synchronized with the external radiation pulses e.g. the laser pulses in the visible-NIR-MIR range, the THZ radiation pulses, or the higher order harmonics of the laser pulses (HHG) etc., thus the perturbation to a system by a 'Pump' pulse could be measured by a 'Probe' pulse, to reflect the dynamics of electrons, atomic lattices, molecules, and photochemical or photo-catalytic reactions etc. of the system, within the ultrafast time scales. Therefore measuring and monitoring the time delays between the X-ray FEL pulses and the external radiation pulses, as well as the detailed structure of X-ray pulse profiles at the shot-by-shot basis are in great demand.

2 Strategy for the Development of European XFEL Photon Temporal Diagnostics

The XFEL.EU is a giant research facility includes: i) the injection laser and RF electron gun system, the super-conductive linear accelerator (LINAC) to create and accelerate electrons to the relativistic energy of >10 GeV; ii) three X-ray undulator systems to generate X-ray photons in different wavelength ranges and with extremely high beam brilliance, through the self-amplified-spontaneous-emission (SASE) process; iii) three X-ray photon beam transport systems; and eventually iv) six scientific instrumental end-stations oriented for various research topics [2]. The three SASE undulators will create X-ray free-electron-laser pulses with photon energy from the soft X-ray range of ~0.3 keV photon energy up to the hard X-ray range of > 20 keV photon energy. Benefiting from the technology of the super-conductive LINAC, the European XFEL could operate not only in the base-line repetition rate of 10 Hz, but also in the 'Burst Mode', where within each fundamental repetition cycle (100 ms in time domain or 10 Hz in frequency domain) an electron bunch train could include up to 2700 intra-bunch pulses having the intra-bunch repetition rate of 4.5 MHz and lasting ~600 μs (refer to Fig. 2.1). Generally, the machine is operating in the nominal bunch charge mode, possessing ~1 nC electron charge, which could generate the SASE X-ray photon pulse duration of a few tens of femtoseconds. On the other hand, the machine could also be set to work in the low bunch charge mode of ~20 pC, which is expect to deliver the extremely short SASE pulse of 1-2 fs or even down to the atto-second regime [2].

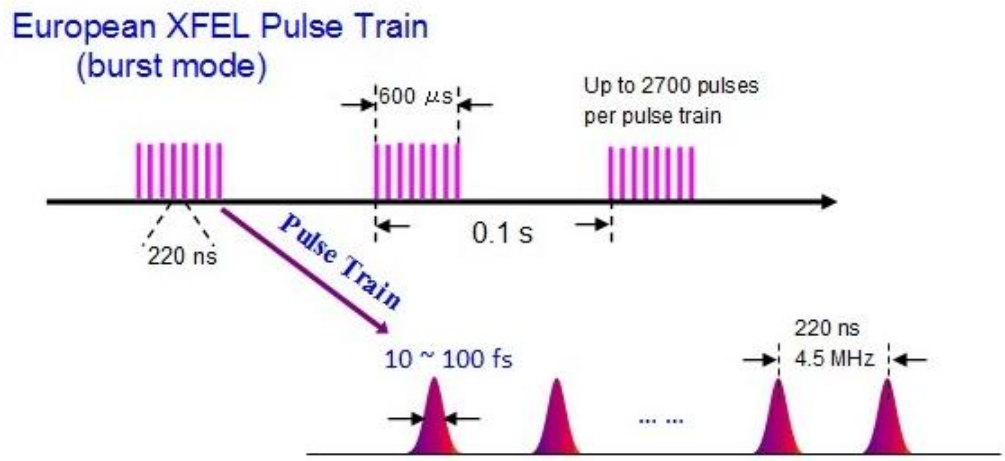

Fig. 2.1 *The temporal structure of the burst mode operation of the European XFEL.*

The X-ray photon diagnostics, including the temporal diagnostics are in demand, to cover the broad range of X-ray photon energies of European XFEL and to measure various XFEL photon pulse profiles under different operational conditions, however it is really difficult and not practical to develop a universal X-ray photon temporal diagnostic device which could work effectively for all different circumstances. Ideally the European XFEL photon temporal diagnostics would be multiple types of devices and each of them works most effectively only within certain X-ray photon energy range. And their applicability to the extremely high beam intensity and compatibility to the high-repetition rate burst-mode operation require additional assessment. Especially the investigation and development of the X-ray photon temporal diagnostic techniques have been conducted in most recent years, and still remain as very challenge topics. Various sophisticated experimental schemes & techniques utilizing the advanced and state-of-the-art instruments are still under investigation. The realization of the reliable and robust X-ray photon temporal diagnostics with better temporal resolution will certainly depend on the success of these frontier research topics. And apparently, different approaches would require the expertises from different research fields, and would need substantial amount of endeavour and man power. Our primary strategy is staying on the updated status of these on-going projects and developments, trying to get involved in the relevant research campaigns, and eventually selecting the most appropriate techniques and methods for the specific photon beam lines and the scientific instrument end-stations of European XFEL. Besides that, the ideal X-ray photon temporal diagnostics

should be as simple as possible, user-friendly, and easy to operate, having long-term stability and reproducibility, requiring minimal effort and cost for the routine operation and maintenance.

As introduced previously, European XFEL will be operated in the base-line repetition rate of 10 Hz with the flexibility to the burst mode operation of the highest repetition rate up to 4.5 MHz. In order to achieve the single-shot measurement within the XFEL intra-bunch pulse train, the relevant devices and diagnostics would have to complete a data acquisition – storage and system recovery cycle within ~220 ns. However not all the devices are able to do that, especially those X-ray photon temporal diagnostics, which acquire the high resolution images or implement a long Time-of-Flight (TOF) tube to differentiate and measure the electron/ion kinetic energies, usually require longer times for a data-acquisition cycle thus can only work at slower rates, therefore only selected X-ray pulses derived from the burst mode electron bunch train could be used. In the meantime, different cases associated with various X-ray photon energies, X-ray beam intensities and different absorptions/attenuations when using different materials etc. need to take into account to avoid the problem of the heat over-loading and the damage to the diagnostics.

3 The Temporal Properties of European XFEL Photon Pulses

The X-ray photon beam parameters of European XFEL SASE1 to 3 are summarized by [2, 3]. The X-ray photon pulses are generated via driving the electron bunch (where the electrons are travelling at the ultra-relativistic velocity with kinetic energy >10 GeV) through the three different undulator segments SASE1-2 and 3. While propagating down through the undulator segments formed by a long array of alternative magnetic poles, the electron bunch is vibrating as a shallow sinusoidal trajectory to give off “synchronized” radiation, interacting with and modulated by its own radiation through the aforementioned SASE process, therefore the originally small and random-phase radiation noise would be amplified to a few orders higher till achieving the saturation. With proper optimization of the electron bunch properties (e.g. the bunch charge peak current, the beam longitudinal & transverse profiles, the beam emittance, and the electron kinetic energy spread etc.), the saturated FEL radiation pulse would possess highly transverse coherence and partially longitudinal coherence, where the longitudinal profile of the FEL pulse includes many individual coherent spikes which are mutually un-correlated and incoherent. The radiation pulse profile is correlated to the electron bunch length and bunch charge peak current. The optimal peak current is usually chosen as ~5 kA, thus for the nominal high bunch charge mode of ~1 nC, the electron bunch length is around 180 fs; for the low bunch charge mode of ~20 pC, the bunch length is as short as ~2.8 fs. The suggested European XFEL electron bunch durations are given by Table1 in [2] at quite a few circumstances, thus the SASE radiation pulse is temporally confined within the electron bunch duration and shorter than the bunch length. The photon pulse duration is mainly as a function of the bunch charge, relatively independent with the electron kinetic energies i.e. the radiated X-ray photon energies. And the minimal SASE pulse duration is restricted by Heisenberg Uncertainty Law (or Transform Limit): $\tau_X \approx \frac{1}{\Delta\omega_s}$, where $\Delta\omega_s$ is

the spectral bandwidth of an individual coherence spike in the SASE radiation spectrum (as demonstrated in Fig. 3.1 (b-c)).

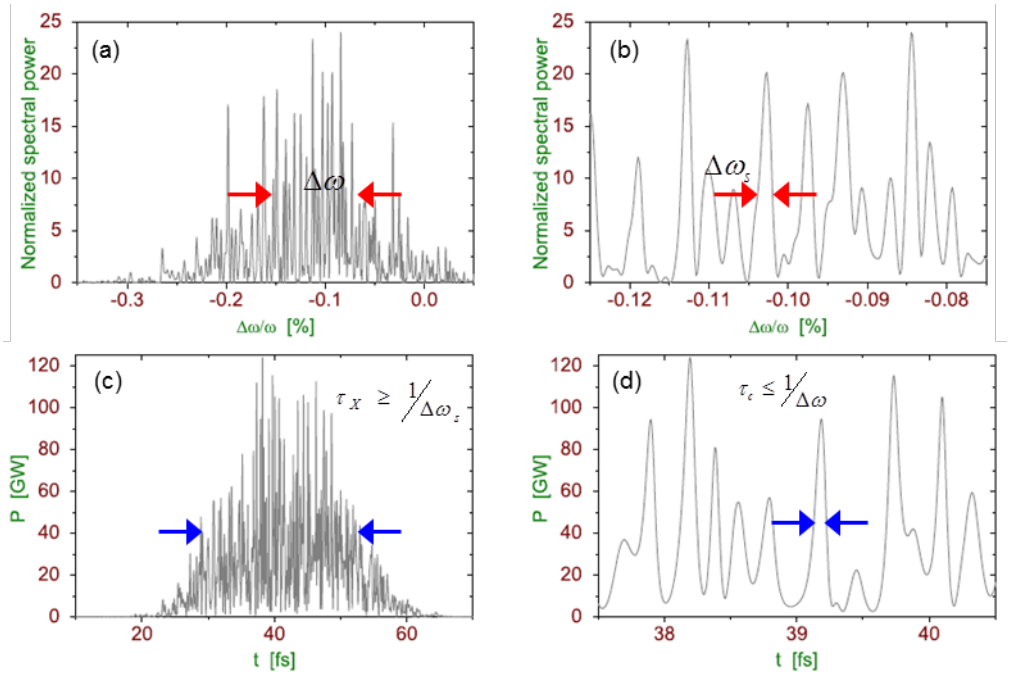

Fig. 3.1 *(a) and (b) (zoom-in) the spectral structure of the radiation pulse from European XFEL SASE1 (or 2). Electron energy is 14 GeV, bunch charge is 250 pC, and the photon energy is ~8.3 keV. (c) and (d) (zoom-in) are the corresponding temporal structure of the radiation pulse (from [3]).*

The radiation pulse length can only reflect the coarse temporal structures of the X-ray SASE pulse. As introduced previously, the SASE pulse actually includes from a few up to a few hundred coherent spikes (determined by the bunch charge mode), and any two of those individual spikes in a SASE pulse are in-dependent and non-correlated each other (as shown in Fig.3.1 (c-d)). The upper limit of the SASE pulse coherence time (reflecting the degree of the longitudinal coherence) is given by the transform limit of the X-ray spectrum (i.e. the radiation spectral bandwidth or wavelength bandwidth) as:

$t_c \approx \frac{1}{\Delta\omega} = \frac{\lambda}{c}\left(\frac{\lambda}{\Delta\lambda}\right)$, where Δω is the spectral bandwidth of the overall SASE radiation spectrum (Fig.3.1 (a) & (d)), λ and Δλ are the corresponding X-ray wavelength and wavelength bandwidth respectively.

The fundamental radiation wavelength in an undulator with a period of λ_u is $\lambda = \frac{\lambda_u}{2\gamma^2}\left(1 + K_{rms}^2\right)$. Where $K_0 = \frac{eB_{\max}\lambda_u}{2\pi \cdot m_e \cdot c} = 0.934 \cdot \lambda_u[cm] \cdot B_{\max}[Tesla]$ is called the undulator parameter, K_{rms} is its rms-value (e.g. for the linear polarized radiation field $K_{rms} = K_0 / \sqrt{2}$). And $\gamma = E_e / (m_e c^2)$ is the relativistic factor, for example when the electron kinetic energy is about $E_e \approx 10.5$ GeV, γ is ~20548, which explains why using the undulator period in tens of millimeters could generate hard X-ray radiation in Angstrom or sub-Angstrom wavelength.

Moreover, the SASE radiation properties could be calculated in the framework of one-dimensional model approximately [4], where the 1D Pierce parameter is given by,

$$\rho_{1D} = \frac{\lambda_u}{4\pi}\left[\frac{4\pi^2 j_0 K_{rms}^2 A_{jj}^2}{I_A \lambda_u \gamma^3}\right]^{1/3} \qquad (3.1).$$

And the SASE gain length in the undulator is,

$$L_{G0} \approx \lambda_u / \left(4\pi \cdot \sqrt{3} \cdot \rho_{1D}\right) \qquad (3.2).$$

The saturation power gain is by,

$$G \approx \frac{N_c}{3}\sqrt{\pi \cdot \ln N_c} \qquad (3.3).$$

Where $N_c \sim I_0 / \left(e\rho_{1D}\omega\right)$ is associated with the number of co-operating electrons to give off the coherent radiation spike in the SASE pulse.

Eventually the coherence time for a SASE pulse calculated by the 1D model at the saturated gain is,

$$t_c \approx \frac{\lambda}{\rho_{1D} \cdot 2\pi c}\sqrt{\frac{\pi \cdot \ln N_c}{18}} \qquad (3.4).$$

Among the above formulas, the 1D Pierce parameter ρ_{1D} could directly reflect the radiation spectral band-width by $\rho_{1D} \sim \frac{\Delta E_{\hbar\omega}}{2E_{\hbar\omega}}$.

However the 1D model could only give an approximate estimation of the FEL SASE power gain and growth in the undulator, in a practical FEL design, the electron bunch energy spread, the bunch charge emittance and the radiation beam diffraction limit factor etc. would need to be considered too, then the radiation power gain length substantially increases due to the deterioration of the electron bunch properties during the SASE process: $L_G \approx L_{G0}(1+\Lambda)$ [4, 5]. The more accurate modeling for the FEL gain process in the undulator could carried out by the 3D simulation packages, e.g. GENESIS [6, 7].

The calculated coherence times for European XFEL are summarized in Table 5 for the Soft X-ray beam line SASE3, and Table 6 for the Hard X-ray beam line SASE1 or 2 in [2]. The general features are: i) the X-ray photon energy is higher (i.e. shorter wavelength), the coherent time is shorter. ii) at the same radiation wavelength, the higher bunch charge mode is associated with relatively smaller radiation spectral bandwidth, therefore the coherent time increases slightly, from 20% more (for the soft X-ray) up to a factor of 2 (for the hard X-ray). iii) For the harder X-ray (e.g. 24.8 keV) at the low bunch charge mode (e.g. ~20 pC), the coherent time can be shorter than 100 atto-seconds; for the softer X-ray (e.g. 280 eV) at the high bunch charge mode (e.g. ~1 nC), the coherent time can be very long ~1.83 fs. However achieving the time resolution from sub-2 fs down to the atto-second regime for the X-ray photon is still a very challenging technique - no practical diagnostics is available at this moment.

By applying appropriate parameters and implementing the 1D formula in Eq.3.1-3.4 (including the undulator parameter), the values in Table 5 and 6 in [2] could be reproduced.

For example using the following parameters for SASE 3:

Undulator Period: $\lambda_u =$ 68 mm

Electron Peak Current: $I_P = 5$ kA

Electron Beam Diameter: 100 µm

Electron Kinetic Energy: 10.5 GeV

R.M.S. Undulator Parameter: $K_{rms} = 7.38$

Photon Energy: $E_{\hbar\omega} = 278$ eV (~ the lowest photon energy of XFEL.EU)

Then the results in the below could be obtained:

1D Pierce Parameter: $\rho_{1D} \sim 0.0014$

Radiation Gain Length: $L_{G0} \sim 2.25$ m

Cooperating Electron Number: $N_c \sim 5.3\times10^7$

Saturation Length: $L_{sat} \sim 30$ m

Coherent Time at the Saturation: $\tau_c \sim 1.98$ fs

Applying the following parameters for SASE 1 or 2:

Undulator Period: $\lambda_u =$ 40 mm

Electron Peak Current: $I_P = 5$ kA

Electron Beam Diameter: 100 µm

Electron Kinetic Energy: 17.5 GeV

R.M.S. Undulator Parameter: $K_{rms} = 1.20$

Photon Energy: $E_{\hbar\omega} = 29.8$ KeV (at the higher photon energy of XFEL.EU)

Then the following results could be obtained:

1D Pierce Parameter: $\rho_{1D} \sim 0.0002$

Radiation Gain Length: $L_{G0} \sim 9.43$ m

Cooperating Electron Number: $N_c \sim 3.5\times10^6$

Saturation Length: $L_{sat} \sim 110$ m

Coherent Time at the Saturation: $\tau_c \sim 110$ as

So the above calculation could reflect the coherent time of the European XFEL SASE pulses is in the range of ~100 as up to ~2 fs, mainly determined by the radiation wavelength and the bunch charge.

4 Requirements for the X-ray Photon Temporal Diagnostics

4.1 Requirement by the Machine and Timing Distribution System

One of the most important applications of the X-ray free electron laser is to study the ultrafast dynamics within the microscopic structures. It requires the combination of the X-ray FEL pulses and the external radiation pulses (e.g. ultrafast optical laser) as the ‘Pump-and-Probe’ measurement, where the experiment is conducted at various delays between FEL and optical laser pulses, the dynamic changes of the system could be recorded, analyzed and understood. These types of experiments require the high level of synchronization of the FEL and optical laser pulses, and the precise recording the mutual arrival (delay) times of the ‘pump’ and ‘probe’ pulses.

The layout of XFEL synchronization system is plotted in Fig. 4.1. Usually a Master-Laser-Oscillator (MLO) is used to provide a stable timing-reference for the overall system. A mode-locked femtosecond fibre optical laser could be considered and developed as the MLO (e.g. Erbium-doped fibre laser which is lasing at the central wavelength of 1550 nm - also called Telecom wavelength). The timing distribution system is using dispersion-compensated optical fibres to link various components/instruments of the XFEL machine with the MLO. Streams of short optical pulses are sent from the MLO through the optical fibre links to the accelerator sub-systems, and then they are sent back through the same fibre for the stabilization purposes. By correlating the arrival-time of the return pulses with the pulses directly output from the MLO end, the round trip could be maintained constant via modifying the length of the optical fibre. Thus the XFEL subsystems and instruments are all locked and synchronized to a common timing reference precisely. However due to the fact the X-ray free electron laser is a giant facility, the longest round trip could be around ~7km, corresponding to ~100 intra-bunch pulses in the burst

mode. So corrections for the short-term instability of the link end-station cannot be made, and would eventually impact on the final synchronization precision. The synchronization scheme of the XFEL timing distribution system includes two big categories: one is the optical-to-electronic synchronization; the other is the optical-to-optical synchronization. For the former, the electron bunch arrival-time with respect to the optical pulse in the optical fibre link can be detected from a simple pickup with broadband electro-optical modulators (EOM). EOMs can also be used to precisely detect the phase of the acceleration RF in superconducting cavities, via sampling the RF with the laser pulse-stream of the timing reference system. The latter is mainly related to the measurement of the arrival time of the X-ray laser pulses at the experimental end-station through the direct optical-to-optical cross-correlation method, which is usually more concerned by the user groups, would be the focus and central topics of the next section.

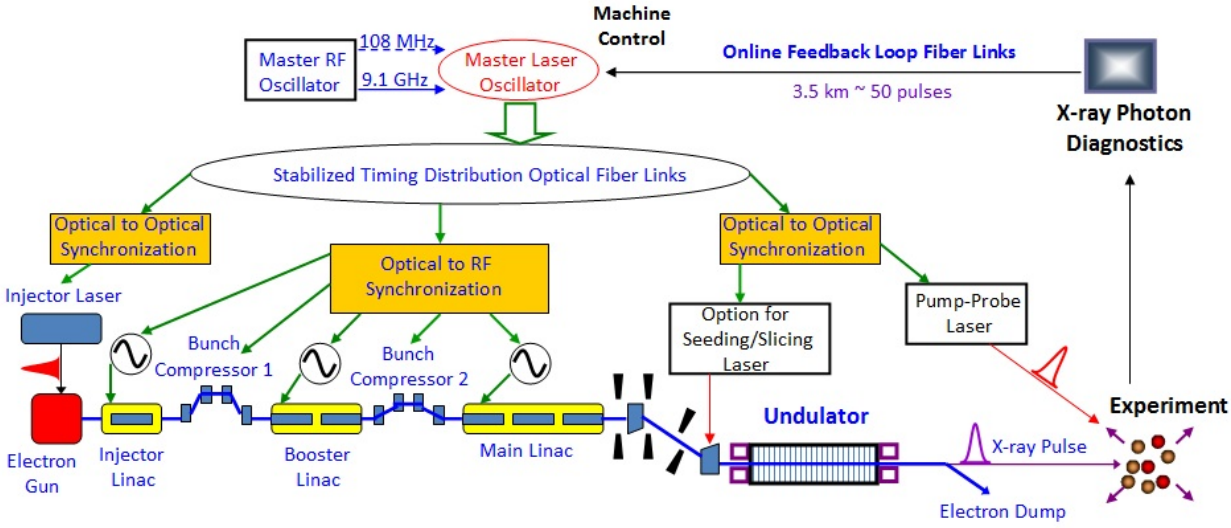

Fig. 4.1 *The schematic outline for the timing distribution and synchronization system, and the on-line X-ray photon diagnostic feedback loop for the European XFEL is also included.*

The European XFEL could work at different bunch charge modes, from the low bunch charge mode of ~20 pC, up to the nominal bunch charge mode of ~1 nC. The SASE X-ray pulse duration is mainly determined by and confined within the electron bunch length. The shortest bunch length to achieve is essentially related to the bunch charge and the bunch length compression. The European XFEL Linac beam line would install 2 Chicanes (electron

bunch compressor) located at two different intersections of the LINAC, and associated with the electron kinetic energy of ~0.5 GeV and ~2 GeV respectively (Fig.4.1). The optimal compression through the sequences of LINAC electron accelerators and two Chicanes leads to the electron bunch lengths of ~3 fs for the low bunch charge mode (~20 pC), and 100~200 fs for the high bunch charge mode (~1 nC) respectively.

After the European XFEL is commissioned towards the end of 2015, it should provide the flexibility to satisfy the varieties of the user requirements, e.g. the tunability of the photon energies and photon pulse durations during their experiments, through tuning the electron kinetic energies, bunch charges or bunch lengths during the operation. The fast scheme to change the machine configurations and electron parameters within a same bunch train (for a maximal duration of 600 μs) should be possible. Therefore, there is a demand for constructing an X-ray photon diagnostic feedback loop, which could monitor in real-time the X-ray pulse properties (e.g. pulse arrival times and pulse durations) at the X-ray transport system and various experiment end-stations, then directly send the real-time information back to the LINAC subsystems through the on-line feedback loop (Fig. 4.1). Upon receiving the feedback signals, the machine control should proceed the on-line tuning, modify and optimize the machine parameters to stabilize its operation and satisfy the demands from users. The optical fibre links are also considered as the feedback loop, the signals are transferred from the user stations all the way up to the machine control/protection system and the injector laser system for a maximal distance of 3.5 km. Providing in the burse mode operation with 4.5 MHz intra-bunch repetition rate, the time for travelling such a distance is corresponding to the delivery of roughly ~50 intra-train electron bunches.

4.2 Requirement from the Instruments and Experimental Users

The X-ray pump-probe experiments and systematically nano-scale & ultrafast dynamics research are able to carry on since the commissioning of FLASH [8] and LCLS [9]. The highly accurate synchronization in between the X-ray FEL pulses and the external laser pulses (including other types of radiation

sources) is absolutely essential for measuring and charactering the ultrafast phenomena and dynamics precisely. The current status regarding to the X-ray FEL operation and measurement in time domain are: the X-ray photon pulse duration could be tuned in the range of a few fs to ~100 fs, and the best temporal jitter calibration at the user experimental station is typically within 10-50 fs. According to the photon temporal monitoring devices at the user station, or directly through some user experiments, generally three types of temporal instabilities have been observed: 1) shot-to-shot jitter, 50-100 fs; 2) short term phase shift (<10 min), 200-300 fs; and 3) long term drift (for the time scale of >10 mins to a few hours, e.g. an experimental shift of 12-hour), a few pico-seconds. The future European XFEL timing distribution system is supposed to monitor both the short and long term signal drifting, and to feedback those signals via the optical fibre links to the machine controls (including MLO) located at a few kilometres away, then the machine should immediately proceed the on-line real time tuning and optimization. This could happen in a very short time scale (e.g. within the duration of a same bunch train of 600 μs). The shot-to-shot beam intensity/spectral fluctuation and temporal jitter of FEL limit the temporal resolution of the measurement of the ultrafast dynamics. At the optimal scenario, the temporal resolution down to 20-30 fs has been successfully achieved. However retrieving the shot-by-shot jitters usually takes a long and tedious procedure as the post-experiment sorting process. The future projects such as the Seeded-FLASH and LCLS II, are referring to the seeded FEL sources and setting the target to achieve a jitter time of < 5 fs for the single-shot measurement, which would eventually enable the ultrafast e.g. few-femtosecond or atto-second research topics. The European XFEL will also have the flexibility to operate at the low bunch charge mode to generate the X-ray pulses < 1 fs duration (composing only a few coherent spikes). And for the long run, the seeded XFEL will also be considered and developed for the soft X-ray beam-line SASE3, and eventually for the hard X-ray beam-line SASE1-2 as well. Therefore the ultimate goal for the X-ray photon temporal diagnostics is to develop a series of devices which could provide super-accurate temporal resolution and robust performance for various ranges of the X-ray photon energies.

European XFEL would construct six scientific instrument stations: Single Particle, Clusters and Bio-molecules (SPB), Femtosecond Xray Experiments

(FXE), Materials Imaging and Dynamics (MID), High Energy Density Science (HED), Small Quantum System (SQS), and finally Spectroscopy and Coherent Scattering (SCS) [2]. Among them the FXE (with hard X-ray of 5-20 keV) and SQS (with soft X-ray of 0.3 – 3.0 keV) are most related to investigate the ultrafast phenomena and dynamics, therefore they will need the X-ray photon temporal diagnostics to measure and calibrate the X-ray photon temporal profiles, and to synchronize the XFEL/optical laser pulses for the experiments. So the reasonable strategy is to coordinate with the responsible instrument scientists and figure out their exact requirements and demands, and try to formulate a collaborative development plan and eventually commission the parasitic temporal diagnostic devices located near to or within the instrument stations. The temporal diagnostics may be located at the down-stream of the Kirkpatrick-Baez (KB) focus mirror, therefore various signal levels i.e. dynamics range, S/N ratio and compatibility of the devices to various beam intensities (i.e. the beam sizes) should be taken into account. And the diagnostics should also include the beam spatial-overlapping monitor, and as well as the unit for the coarse-delay searching and monitoring. Since the FXE instrument will use the hard X-ray photons of 5-20 keV [10], so this type of temporal diagnostics could be an on-line non-invasive device in transmission fashion, located at the upper stream of the experimental chamber. While for the SQS end-station which is operated in the soft X-ray range of 0.3-3 keV [11], the experimental sample is usually in gaseous phase/liquid jet or in molecular particles/clusters, it may be more appropriate to build up the parasitic timing diagnostics at the down-stream of the experimental interaction region. Therefore the sample for the diagnostic device could be a bulk material, as an opaque and invasive fashion.

5 X-ray Photon Temporal Diagnostic Methods and Techniques

Measuring the X-ray pulse profiles usually refer to the advanced state-of-the-art techniques, most of them are being investigated and developed during recent years. In order to realize the robust and persistent X-ray photon temporal diagnostics for routine operation, tremendous work is still yet to be done. The X-ray photon temporal diagnostics can be differentiated into two major categories: 1) the X-ray photon pulse length measurement device; 2) the X-ray photon pulse arrival monitor. The former is used to measure the X-ray photon pulse duration as well as the longitudinal radiation power distribution in a SASE X-ray pulse; the latter is mainly regarding to characterization of the time-delay and shot-by-shot temporal jitters for the X-ray pump-probe experiment, which is absolutely important for the measurement of the ultrafast dynamics referring to the X-ray waves.

5.1 X-ray Photon Pulse Length Measurement Technique

5.1.1 X-ray Auto-Correlator

The direct method to measure X-ray photon pulse duration is to design and fabricate an X-ray auto-correlator, such a device in the EUV to XUV range has been developed on the plane grating monochromatic beamline PG2 at FLASH [12]. At this moment, the autocorrelation method for X-ray wavelength, especially for the hard X-ray range e.g. the SASE1-2 beamline of European XFEL is still in development and held back by several major technical challenges.

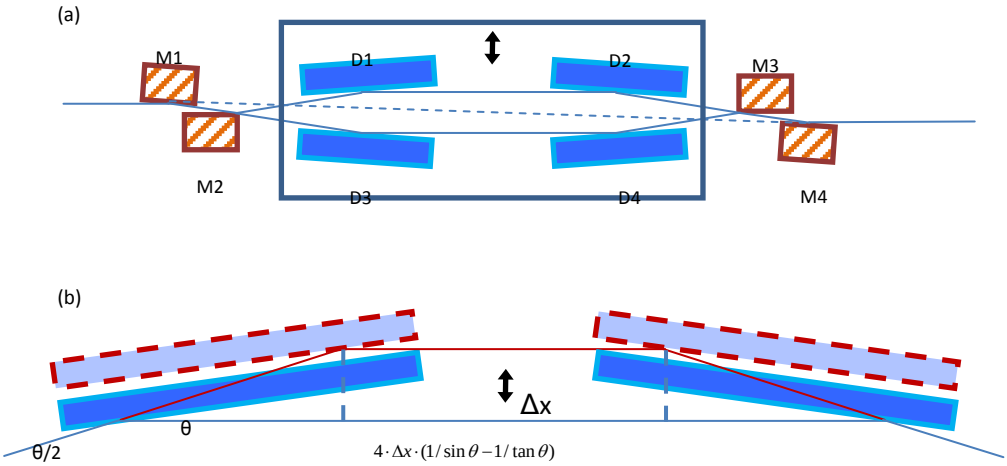

Fig.5.1 *(a) Schematic layout for a typical X-ray auto-correlator utilizing the grazing angle incidence and wave-front splitting delay generation. (b) The effective delay corresponding to the transverse scanning motion in the split-delay unit.*

An X-ray auto-correlator device is constructed similarly as a visible light auto-correlator, where a beam is split into two identical replicas through a split-delay unit (SDU) and the mutual delay between these two replicas were generated via a scanning stage and then eventually recombined to create a non-linear signal, from which the photon pulse duration as well as the phase information could be retrieved and determined. The optical design of a typical X-ray auto-correlator is given in Fig. 5.1 (a), where all the mirrors are Si-substrate with CVD diamond coating, with surface polishing of < 1 nm. The mirrors M1 to 4 are fixed, among them M1&4 are the beam path preserving mirrors and M2&3 are the beam splitting & recombining mirrors. The mirrors D1-4 are located on a scanning stage, and their relative positions and surface orientations are all well-adjusted, aligned and optimized. The grazing angle incidence (e.g. the angle between the beam and the mirror surface is smaller than 2 deg.) is adopted to enhance the overall transmission of the SDU to above 50% for the FLASH wavelength in range of 50nm-7nm [13]. Both of the upper and lower beams in SDU reflect 5 times before they preserve the original beam paths with minor transverse shift (the dash line in Fig. 5.1 (a)). As illustrated in Fig. 5.1 (b) while the delay stage is in scanning motion, the output beam trajectory through the in-coupling mirror D1 (or D3) and the out-coupling mirror D2 (or D4), is still preserved (obviously it would collide at different spots on the mirror surfaces associated with different delay settings).

According to the geometry of the grazing angle incidence, the X-ray beam deviates a small angle θ each time when it reflects off the mirrors D1-4. Therefore the effective delay associated with the transverse scanning of the translation stage Δx is $4 \cdot \Delta x/c \cdot (1/\sin\theta - 1/\tan\theta)$. Providing θ=4˚, the effective delay generated by the SDU is ~465 as/μm. Assuming the precision of the travel of the translation stage is ~1μm, then the minimal delay step of ~0.5 fs could be generated by applying such a mechanical delay stage. Eventually after passing through the SDU, the two half beams are recombined and overlapped spatially (transversely) and temporally (longitudinally) to form the photon source for the auto-correlation via a non-linear process.

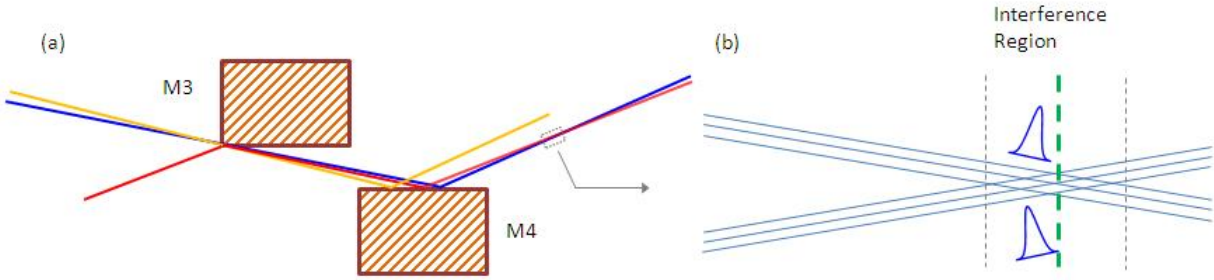

Fig.5.2 *(a) The beam configuration passing through the mirrors M3-4 in the SDU. (b) The two beams over-lap in space and time to form the interference fringe.*

The most typical approach to obtain the X-ray auto-correlation signal is through measuring the interference fringes of the two beams generated via the SDU, where the fringes at the various delays and along with the associated visibilities are recorded for characterizing the details of the X-ray FEL pulse properties i.e. its longitudinal coherence and the distribution of the coherent spikes within a pulse duration. Fig.5.2 (a) shows the magnified section of M3&4 in the SDU in Fig. 5.1 and the beam layout. The red beam reflects off the M3 and M4 sequentially (indicating the lower variable beam path in the SDU), the yellow and blue beams pass around the corner of M3 and reflect off M4 (indicating the upper variable beam path in the SDU) and recombine with the red beam. After the reflection from M4, the yellow beam will divergent from and never overlap with the red beam; however through fine-tuning the mirrors M2 or M3 in the SDU (Fig.5.1), the yellow beam could convert itself into the blue one, which gets around M3 and reflects off M4 and overlaps with the red beam at a certain distance away from M4. The spatial

and temporal overlapping of the two beams is magnified in Fig.5.3 (b), a detector could be placed within the beam interference region to measure the fringes and characterize the fringe visibilities at different delays. If both of the two beams (e.g. the wavelength of 23.9 nm i.e. the photon energy of 51.8eV) are collimated, with a rather small crossing angle e.g. α ~ 1.0 mrad, the fringe separation on the detector could be estimated as:

$$\Delta s = \frac{\lambda}{2 \cdot Sin(\theta/2)} \approx 24\ \mu m \quad (5.1).$$

As long as the detector is located inside the beam interference range (in-between the two vertical dash lines in Fig.5.2 (b)), the fringe is observable and the fringe spacing is a constant of ~24 μm. However whenever a focused beam (or Gaussian beam) is applied (more likely the case), the fringe spacing at the detector depends on the distance from the beam focus to where the two beams overlap. Usually the auto-correlator could be arranged to a location which is far from the X-ray beam focus, therefore the treatment of using collimation beam is approximately valid. The typical interference signals are given in Fig.5.3, where the higher contrast fringe signal (one the left) is corresponding to the smaller mutually coherent delay of the two replica pulses from SDU (a), and the lower contrast fringe signal (on the right) is associated with the larger coherent delay (b). However when the time delay is approaching or longer than the longitudinal coherence time of the X-ray FEL pulse, the fringe interference would become blurred and invisible. If the vertical integration is applied to the CCD images of the fringe in Fig.5.3, a series of one-dimensional line-profiles could be obtained, which are similar to the simulated signals in Fig. 5.4 for various contrasts of “visibility”.

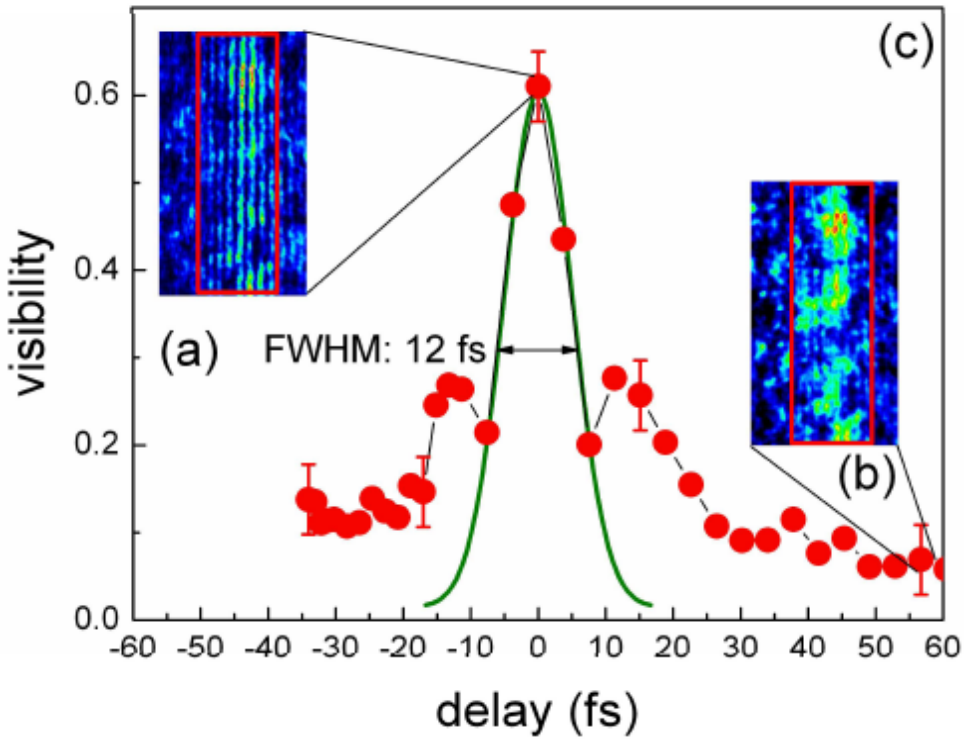

Fig.5.3 *The single-shot interference fringes generated via SDU (a) at the optimal time-delay 'zero", (b) at the large time delay ~55 fs, (c) the visibility of the fringes at various delays are calibrated, and the Gaussian fitting of the 'signal visibility' vs. 'delay' to give the auto-correlation signal and to determine the FEL coherence time. The plot is from reference [12].*

The 1D interference signals in Fig. 5.4 are simulated by the following formula, implementing various values of "visibility", which can be directly reflected by the contrast of the interference fringe in Fig.5.3 [14, 15],

$$I = 2\left(\frac{2J_1(v)}{v}\right)^2 \cdot \{1 + \left|\frac{2J_1(u)}{u}\right| \cdot \cos[\beta_{12}(u) - C \cdot u \cdot v]\} \quad (5.2).$$

Where u and v are the parameters associated with the X-ray beam properties and as well as the details of the imaging system. Generally, the visibility of an interference fringe is defined as,

$$V = \frac{I_{\max} - I_{\min}}{I_{\max} + I_{\min}} = \{2\sqrt{I_1 I_2}/(I_1 + I_2)\}|\gamma_{12}(\tau)| \approx |\gamma_{12}(\tau)| \quad (5.3).$$

As long as the two beams from SDU have equal intensity (which is most likely the case for the typical design of an auto-correlator), the visibility of the fringe V is equal to the absolute value of the coherence $\gamma_{12}(\tau)$ of the light source.

Therefore, the coherence $|\gamma_{12}(\tau)|$ at different time-delays τ could be calibrated by measuring the maximal and minimal intensities of the specific fringes at τ. In Fig. 5.4, the fringe profiles associated with visibility from the nearly full-coherence (close to 1, (a)) to the weak coherence (<0.2, (d)) are plotted. Finally, the coherence at each setting delay is plot in Fig.5.3 (c) as an auto-correlation signal, and the Gaussian fit for the curve near the time-delay zero give the FWHM of 12 fs, corresponding to the longitudinal coherence time of around $\tau_c \approx$ 6 fs.

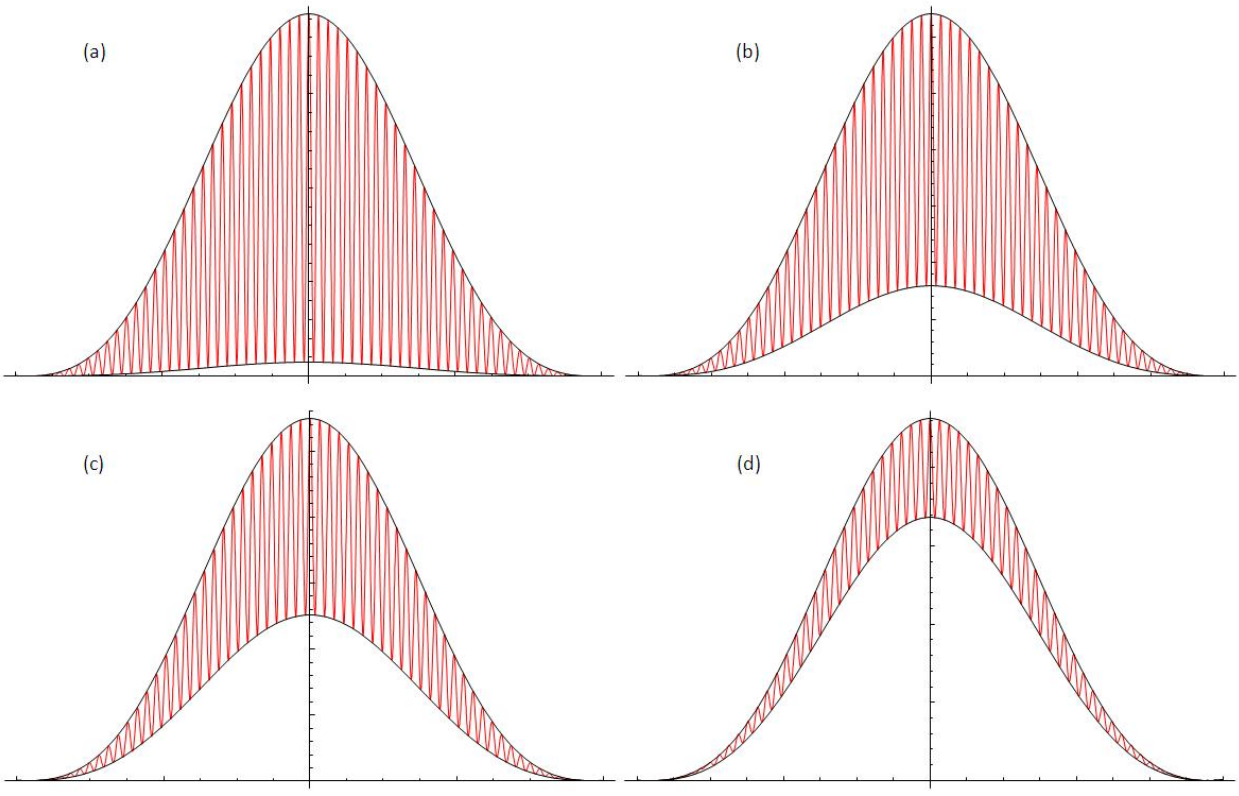

Fig.5.4 *Simulated Gaussian interference fringe for the visibility of (a) 0.93, (b) 0.60, (c) 0.37, (d) 0.16, associated with various longitudinal delays of two replica X-ray pulses.*

In the meantime, the wavefront coherence or transverse coherence of the X-ray pulse could be measured by the similar technique. Not being applied to the SDU device, the collimated X-ray beam is instead sent to a beam blocking screen only leaving two small apertures on the screen. Then the Young's double slits interference fringe would occur behind the blocking screen (here are the double apertures interference though). Changing the

separation of the two small apertures on the blocking screen will be able to explore the wavefront coherence (or transverse coherence) of the beam [16].

Since European XFEL is designed to work at much harder X-ray ranges, the fundamental photon energy of SASE1 or 2 is as high as 12.4 keV, so the primary task is extend and realize the above auto-correlation technique into much harder X-ray photon range. Apparently there are at least two major technical difficulties for the hard X-ray auto-correlation: 1) the gazing incidence angle to the mirror surface with single material coating needs to be very small, thus the diffraction edge effect of the hard X-ray is much stronger compared to the longer wavelength 2) the hard X-ray two-photon non-linear cross-section is extremely small too. For the first difficulty, it requires the beam alignment for the wavefront splitting extremely accurate. Due to the nature of the short wavelength of the X-ray, the refraction index 'n' of the material is typically a bit smaller than that of the vacuum but very close to 1, where $n = 1 - \Delta - i\beta$ (Δ and β are the real and imaginary refraction index modification factors, associated with the boundary condition and X-ray induced plasma distribution within the surface portion, and the X-ray absorption/scattering factors in the atomic structures respectively), so the grazing angle incidence should be smaller than the critical angle:

$$\theta_g = \frac{\pi}{2} - \sin^{-1}(1-\Delta) \quad (5.4)$$

The grazing angle for 12.4 keV photons for amorphous carbon or silicon single crystal coating layer is only 2.4 mrad or 2.5 mrad (< 0.15°) respectively, the beam alignment at this sharp grazing angle incidence is very difficult, and the edge effect would also cause severe diffraction to the beam. Thus it is impractical to design a hard X-ray auto-correlator by using a single crystal (or material) mirror. Nerveless, the simulation by applying a few keV photon energy shows that the multiple thin layers with alternatively higher or lower refractive index material coating structures (e.g. Mo/B_4C, Ni/B_4C) could resolve this problem, where it works similarly as the dielectric mirrors for the light near to the visible range (refer to Fig. 5.5, [17]). Then the optimal reflectivity for the hard X-ray of 2 – 10 keV photon energy in a few degrees could be achieved. However when applying the device to various X-ray photon energy ranges (e.g. for SASE 1 or 2), it would require to change the

grazing incidence angles to accommodate the different X-ray photon energies, so this adds the complicity to the operation of the device. Moreover, the multi-layer structures would introduce the additional dispersion to the X-ray photon pulse, then through reflection from the multi-layer mirror, the X-ray pulse length will be avoidably stretched.

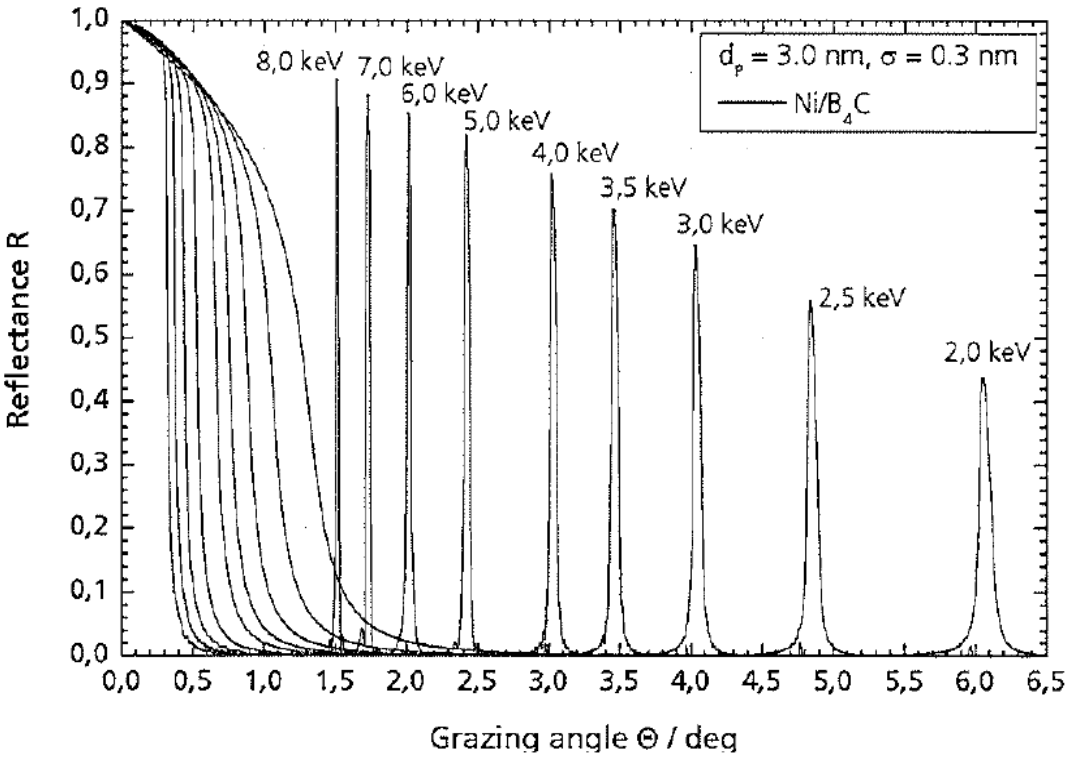

Fig.5.5 *The simulation for the optimal reflectance of the grazing angle incidence at the multi-layer coating Ni/B_4C mirrors for various X-ray photon energies. From the reference [17].*

According to the most recent report by R. Mitzner et al. at Wilhelms - Universität Münster, they are in steps of developing a hard Xray auto-correlation device [17]. The scheme is to implement the grazing angle incidence and wave-front splitting & delay generation technique which has been proved working effectively in the EUV-XUV range, and extend it to the hard X-ray range through the implementation of the multi-layer coating technique. Since the coherence times for SASE1 or 2 are extremely short (100-300 as, which are much shorter compared with that of SASE3, 0.5 – 2 fs), therefore the motion precision of ~1μm for the scanning delay stage moving at ~500as/μm (as given in Fig. 5.1) is insufficient to provide the desired accuracy for the measurement. The scanning stage is suggested to

modify slightly as the one in Fig. 5.6 (a) for the hard X-ray. After the wavefront beam splitting at M2 within the SDU, the lower beam passing through mirror D3&4 located on the scanning stage remains the same as the previous design for the XUV light, to provide the coarse delay of $2\cdot\Delta x/c\cdot(1/\sin\theta-1/\tan\theta)$ ~ 250as/μm (for θ = 4˚). However the upper beam is sent through two mirrors D1&2, which are now mounted on two guide rails; and the track of the guide rail on the left side or right side is set to be perfectly parallel to the incoming or outgoing of the upper beam trajectory (Fig. 5.6 (a)). And in order to preserve the beam path during the motion, the mirrors D1&2 are designed to move together with the same amount: either towards each other to increase the beam path for the upper beam, or outwards to decrease the beam path. As demonstrated by the magnified schematic for the guide rail motion in Fig.5.7 (b), the effective delay is $2\cdot\Delta l/c\cdot(1-\cos\theta)$, and the fine delay tuning of < 20 as/μm (still applying θ = 4˚) could be achieved. This modification in the design of a SDU device would be essential for the hard X-ray beam line of SASE1-2.

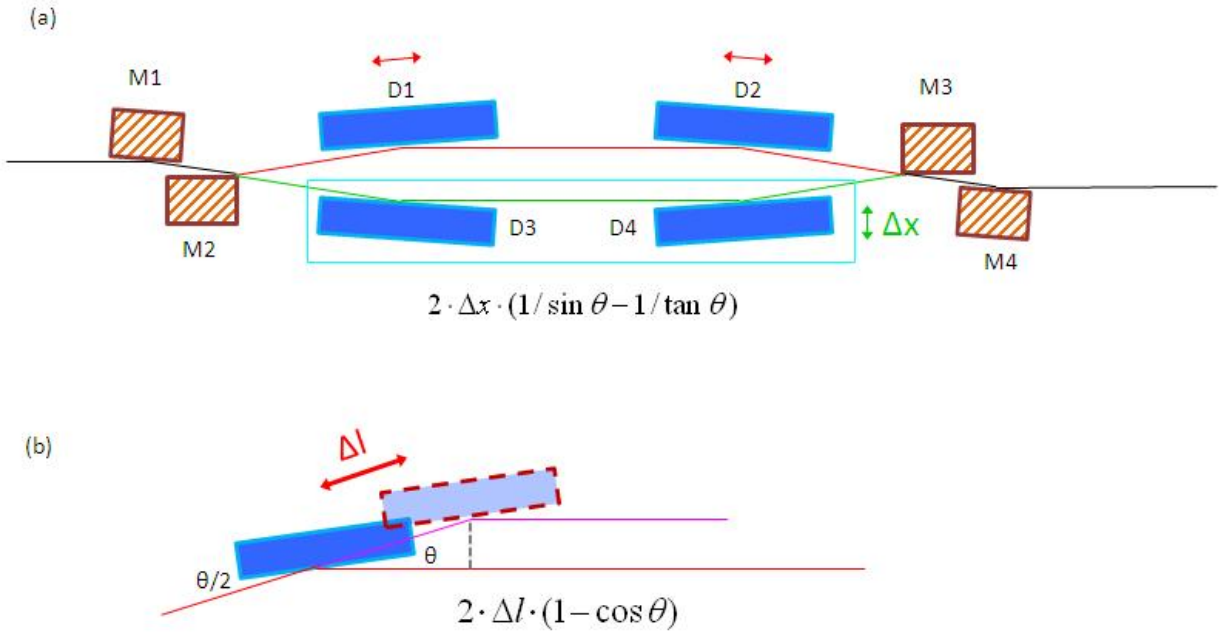

Fig.5.6 *(a) Schematic layout for the hard X-ray auto-correlator design utilizing the guide rail. (b) the effect delay associated with the guide-rail scanning motion.*

And cording to the Eq.5.1, in order to generate the clearly measurable interference fringe (the fringe spacing should be at least larger than the pixel

size of the detector chip) by using the SASE1-2 hard X-ray photon in few Angstrom wavelength, a much smaller crossing angle α of few tens of μrad should be applied, which would significantly increase the length scale of the device, and also the difficulty for measuring the signal at the detector in distance.

5.1.2 X-ray Streaking Technique

X-ray streak camera is a proven tool used in the ultrafast pulse metrology [18]. Within a conventional streak camera, various photocathode materials are exposed to the X-ray pulses to generate the electron pulses to represent the radiation pulses with the identical temporal pulse length. The electron wave-packet is accelerated and transversely deflected by a transiently ramping electric field and the deflection of the electron in the transverse coordinate is recorded by a scintillation screen, which could be calibrated to reflect the temporal duration of the pulse. The time resolution of this scheme is limited by the size of the static image of the electron pulse, its initial electron kinetic energy spread and time-of-flight dispersion, dispersion introduced by the space charge, as well as temporal jitter distribution for individual pulses (if the accumulative acquisition mode is applied). Currently the best time-resolution of the conventional streak camera is >>100 femtoseconds, therefore it could not be applied for measuring the ultrafast X-ray FEL pulses whose temporal durations are within sub-100 fs time scale [19]. The “Streaking” method discussed in this section is utilizing a strong-field long wavelength radiation (from the THz up to the visible light range) as the transverse deflection electric field to emulate the conventional streak camera to characterize the X-ray photon pulse duration [20], where the X-ray “pump” (to trigger the transient ultrafast reactions or dynamics) and THz “probe” scheme (to measure the dynamic signals driven by the X-ray pump pulse) is established to analyze the detailed dynamical features and determine the X-ray photon pulse duration and temporal structures, targeting for achieving the accuracy of down to a few femtoseconds.

The THz field could be generated through a THz undulator located right after the X-ray undulator, therefore the same electron bunches are used to create the X-ray and THz radiation pulses, they are mutually correlated and the synchronization in-between the X-ray and THz pulses could be well

maintained (e.g. below 5 fs). U. Frühling & M. Drescher et al. [21] implemented this method to measure and characterize the XUV photon pulse duration at FLASH experimental station. The layout of the experimental set-up is illustrated in Fig. 5.7 (a), the X-ray pulses and terahertz pulses were collinearly overlapped in the interaction region, where the two beams have orthogonal polarizations (the X-ray field having the horizontal polarization and the THz field having the vertical polarization respected to the laboratory floor). The THz beam line includes a delay apparatus to create various time-delays in-between the X-ray and THz pulses, and is focused by an off-axis parabolic mirror to a 0.3 mm spot size at the interaction region. The XUV beam is reflected by a re-focusing Mo/Si multilayer mirror to generate the spot size of <100 μm in the focus region after passing through a small central hole in the parabolic mirror. The pulse energies of the XUV and THz field could be tuned to 0.2 μJ and 2 μJ respectively for the best performance. In this example, a krypton gas target was supplied by a gas nozzle into the X-ray/THz beam-focus region. The energies of photoelectrons resulting from the ionization of krypton atoms by the XUV excitation were measured by two electron Time-of-Flight (TOF) spectrometers, one has the TOF axis paralleled to the polarization of the THz field, and the other has the axis perpendicular to the THz polarization.

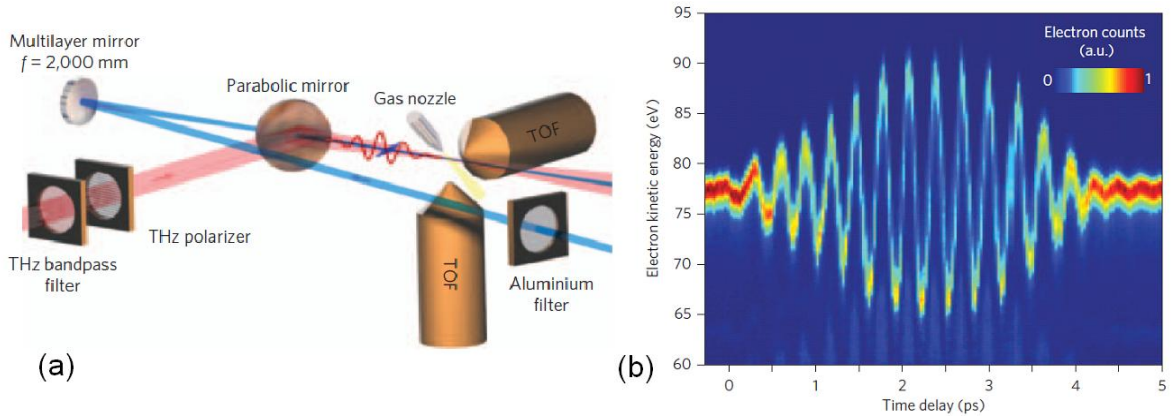

Fig. 5.7 *(a) Schematic of the experimental setup for the X-ray ionization response in the presence of THz streaking field. (b) The representative electron energy streaking signals for various time delays of the X-ray/THz pulses. (From reference [21]).*

Through the investigation of the photo-electron dynamics under the presence of the XUV ionization field and the THz streaking field, the electron

momentum and kinetic energy could be calculated, and the electron final kinetic energy associated with the geometry and the strength of the THz radiation field could be denoted as [22],

$$W(\theta,t) = W_0 + 2U_p \cdot \sin^2(\varphi_i) \cdot \cos(2\theta) + \sqrt{8W_0U_p} \cdot \sin(\varphi_i) * \cos(\theta) \quad (5.5).$$

Where $W_0 = \hbar\omega_{XUV} - E_B$ is the initial kinetic energy of the photoelectrons upon the ionization but without applying the THz field, $U_p = \frac{e^2E_0^2(t)}{4m_e\omega_{THz}^2}$ is the ponderomotive potential of the THz field of $E_0(t)$, φ_i is the phase of the THz field at the instance of the ionization, and the θ is the crossing angle between the electron TOF detector axis and the polarization of THz field. The second and the third terms on the right side of the above equation are corresponding to the ponderomotive and the streaking contributions to the electron kinetic energy shift in the THz field respectively. Applying the THz parameters in the experiment, THz pulse energy 2 μJ, beam focus size 0.3 mm and pulse duration of ~ 1ps, the THz beam intensity and field strength can be calculated as,

$$I = \frac{1}{2}c\varepsilon_0 E_0(t)^2 \approx \frac{2.0\times10^{-6}J}{1\times10^{-12}s} / \left(1/4\cdot\pi\cdot(0.03cm)^2\right) \sim 2.83\cdot10^9 W/cm^2$$

$$E_0(t) \approx 146 MV/m$$

So the ponderomotive potential U_p of the THz pulse is around 2.2 eV.

The mean kinetic energy of photoelectrons from the Kr 4p shell upon the X-ray (13.5 nm, 91.8 eV) excitation without applying the THz streaking field is,

$$W_0 = \hbar\omega_X - W_{bind}(Kr4p) = 91.8 - 14.1 \approx 77.7\ (eV) \quad (5.6)$$

And the relative strength of the streaking energy to the ponderomotive potential can be evaluated as,

$$\frac{\Delta W_{streak}}{\Delta U_p} >> \frac{\sqrt{8W_0U_p}}{2U_p} = \sqrt{\frac{2W_0}{U_p}} \approx 8$$

So under the current experimental conditions, the streaking effect is one order higher compared to the ponderomotive potential, and it would be the dominant factor to change the kinetic energy of the photoelectrons during the

process. For simplicity, the photoelectron spectra measured by the TOF spectrometers with axes parallel (θ=0) or perpendicular (θ=pi/2) to the polarization of the THz field could be assigned as the streaked or non-streaked signals respectively,

$$W(t)_{streak} = W_0 + 2U_p \cdot \sin^2(\varphi_i) + \sqrt{8W_0U_p} \cdot \sin(\varphi_i) \qquad (5.7)$$

$$\text{and} \quad W(t)_{non-streak} = W_0 - 2U_p \cdot \sin^2(\varphi_i) \qquad (5.8).$$

Furthermore, the energy shift of the streaked electrons (which can be considered as a linear acceleration motion towards the TOF detector since $\theta \approx 0$, providing the detector aperture is small enough, then the differential cross section is small) within the THz radiation field having phase φ_i at the instant of ionization is,

$$\Delta W_{//}(t) \approx \sqrt{2W_0 / m_e} \cdot eA_{THz}(t) \qquad (5.9).$$

$A_{THz}(t) = \int_t^\infty E_{THz}(t')dt'$ is the vector potential i.e. the integration of the terahertz field upon the X-ray induced ionization occurs at the time *t*, till the electrons are moving out of the interaction region. Therefore, it is possible to directly map the vector potential of the THz field by measuring the energy change of the streaked photoelectrons. Fig.5.7 (b) shows the energy spectroscopy of the photoelectrons detached by the XUV pulses in the presence of an intense terahertz field at various time delays, which can be fitted by a Gaussian function multiplied by a Sinusoidal THz wave. Here we pre-assumed the streaking condition $\tau_X << T_{THz}/2$ is satisfied (where τ_X is the XUV pulse duration and T_{THz} is the period of the optical cycle of the THz pulse). However when $\tau_X \geq T_{THz}/2$, the streaking features will be washed out and replaced by the averaged sideband signals located beside the central peak of 77.7 eV in the photoemission spectrum (discussed in section 5.2.4). The THz oscillation period of ~306 fs in Fig.5.7 (b) is associated with the frequency of 3.3 THz and the wavelength of 92 μm. And the streaking strength can be evaluated as the time-derivative of the curve $\Delta W_{//}(t)$, which has its peak values (either maximum or minimum) at the a zero crossing of $A_{THz}(t)$,

$$s = \frac{\partial(\Delta W_{//})}{\partial t} = e\sqrt{2W_0 / m_e} \cdot E_0(t)_{THz} \approx 0.7eV \cdot fs^{-1} \quad (5.10).$$

By using the formula discussed above and implementing the THz radiation parameters, the streaked spectra of Kr 4p photoemission electrons upon the FLASH XUV pulse excitation (13.5 nm, 91.8 eV) could be calculated as in Fig. 5.8, where only the 4p electrons are concerned. Not difficult to find out, compared to the non-streaked spectrum, the streaked spectra would be broadened by the THz field, the broadening of the spectral bandwidth is determined by the relative phase of the ionization within a single optical cycle of the THz field. When the phase delays are pi/2 or 3pi/2, the streaking broadening is minimal, but it is corresponding to the maximal change of the electron kinetic energy. While the phase delays are 0, pi or 2pi (associated with the THz vector potential zero-crossing), the streaking broadening is maximal however corresponding to the minimal change of the electron average energy. The streaked spectra with the largest broadening effect could be used to analyze the X-ray pulse durations as well as its temporal properties. Here the only problem is the binding energies of the Kr 4s and 4p valence electrons are quite close, therefore their streaked spectra would possibly overlap, which makes it difficult to analyze the signals and to retrieve the X-ray pulse information. So it might be necessary to use a less intense THz field to generate the distinguishable streaking signals.

According to the previous discussion, in order to determine the pulse duration of the X-ray FEL, the phase delay between the X-ray and THz pulses is supposed to set at a value corresponding to the zero crossing of the signal $A_{THz}(t)$ (refer to Fig.5.8 (b) and the phase φ_i of 0, pi or 2pi), then the photoelectron spectra were measured by two electron energy TOF detectors with axes parallel or perpendicular to the polarization of the THz field as in Fig.5.7 (a). Therefore the non-streaked (perpendicular) and streaked (parallel) single-shot photoelectron spectra could be measured at the same time, and those at the zero transition of $A_{THz}(t)$ (associated with the largest spectral broadening) could be selected and calibrated. As given in Fig. 5.9, the streaked spectrum is discernibly broadened compared to the non-streak spectrum.

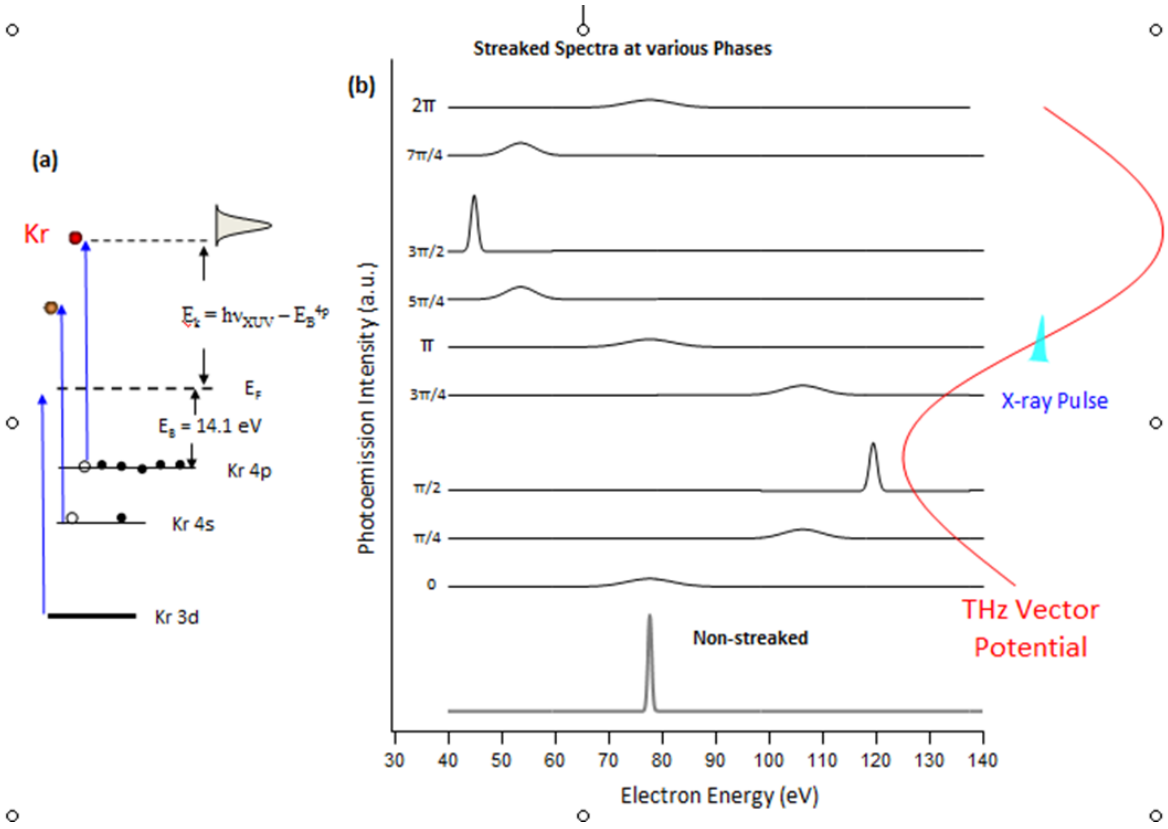

Fig.5.8 *(a) Valence band photoemission in the Kr atom (b) The simulated Kr 4p photo-emitted electron streaked spectra in the presence of an intense THz field, with different relative phases of Kr ionization within the single cycle of a THz pulse.*

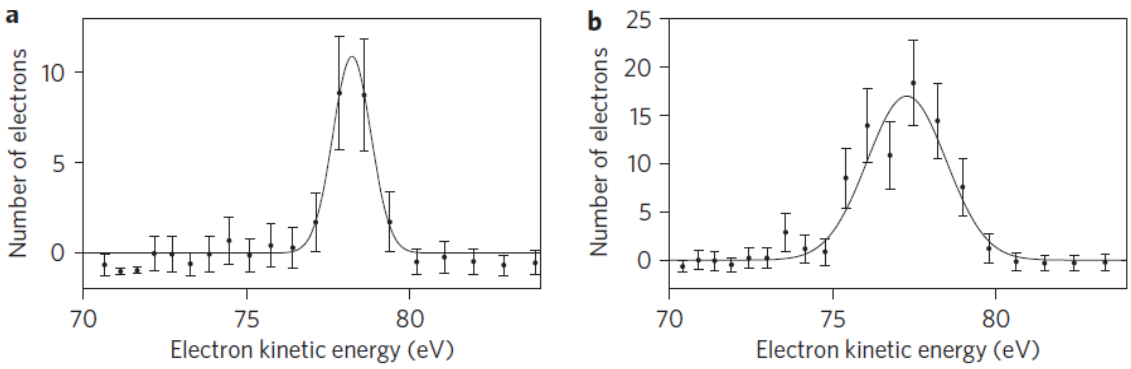

Fig.5.9 *(a) the non-streaked and (b) streaked photoelectron spectra for a single-shot measurement, from [21].*

Assuming a linear chirped Gaussian X-ray pulse

$E_X(t) = E_X^0 e^{-a(t-t_0)^2} e^{i[\omega_0(t-t_0)+c(t-t_0)^2]}$, the r.m.s. spectral bandwidth can be calculated quantum-mechanically for the non-streaked and streaked

spectrum respectively, where c is the linear chirp value and the s is the streaking strength introduced previously (Eq.5.10),

$$\sigma_{X-0} = \sqrt{\frac{a^2 + c^2}{a}} \text{ and } \sigma_{X-streak} = \sqrt{\sigma_{X-0}^2 + \tau_X^2 (s^2 \pm 4cs)}\,.$$

Where the symbol of $\pm$ denotes the sign of THz electric fields which change for every successive adjacent zero crossing of $A_{THz}(t)$, where the time delay between XUV and THz field changes the half of a THz optical cycle, i.e. 153 fs for this example. A large number of single-shot streaked spectra (e.g. 1000 shot) could be measured for two consecutive zero transition of $A_{THz}(t)$, and a de-convolution scheme is as following,

$$\left(\sigma_{deconv}^2\right)_1 = \sigma_{X-streak}^2 - \sigma_{X-0}^2 = \tau^2 (s^2 + 4cs)$$
$$\left(\sigma_{deconv}^2\right)_2 = \sigma_{X-streak}^2 - \sigma_{X-0}^2 = \tau^2 (s^2 - 4cs)$$

Therefore the average X-ray photon pulse duration can be determined as,

$$\bar{\tau}_X = \sqrt{\frac{\left(\bar{\sigma}_{deconv}^2\right)_1 + \left(\bar{\sigma}_{deconv}^2\right)_2}{2s^2}} \quad (5.11).$$

And the average linear chirp for the Gaussian pulse is,

$$\bar{c} = \frac{\left(\bar{\sigma}_{deconv}^2\right)_1 - \left(\bar{\sigma}_{deconv}^2\right)_2}{8s\bar{\tau}_X^2} \quad (5.12).$$

The streaking method has been demonstrated working successfully in the XUV or soft X-ray range by using the gaseous target. And the accuracy of measuring the X-ray photon pulse duration is mainly determined by the resolution of the electron energy spectroscopy and the streaking strength applied to the system. For the current experimental result discussed in the text [21], the temporal resolution is about 30 fs. However, the streaking technique to characterize the hard X-ray photon pulse duration is currently under investigation and not available till now. The photoabsorption cross-section for the hard X-ray photon in gases is pretty small (usually the core electron - not the valence electron photo-excitation should be concerned), in the meantime gases have less electron density compared to the solid states, therefore it might need to apply the streaking technique at the surface of solid-state samples for the hard X-ray beam [23]. In order to realize the hard X-ray streaking, it also requires to have a high energy electron spectrometer

(up to > 10keV) with high energy resolution, which is a developing and state-of-the-art technology as well.

The optical cycle of the THz field could be a few hundred femtoseconds up to the pico-second time scale (determined by its frequency), however the electron bunch longitudinal duration could be compressed down to below 100 fs, to generate the sub-100 fs SASE THz radiation pulse in the undulator. Therefore the sub-100 fs time duration is only corresponding to the fraction of an optical cycle of the THz radiation field. By applying the appropriate electron bunch parameters and again Eq.3.1 to 3.4, the typical coherence time of a SASE pulse in THz range could be calculated as 100-200 fs, which shows the sub-optical cycle and full coherence THz pulse could in principle be produced by the well-configured THz undulator.

Besides using the THz undulator, an external strong-field high power laser could also be applied to generate THz radiation pulses through the optical rectification process. Optical rectification is related to a nonlinear process, and its optical-to-THz conversion efficiency can be described by the following formula [24]:

$$\eta_{THz} = \frac{2\omega_{THz}{}^2 d_{eff}^2 L^2 I}{\varepsilon_0 n_\omega^2 n_{THz} c^3} \frac{\sin^2(\Delta k \cdot L/2)}{(\Delta k \cdot L/2)^2} \quad (5.13)$$

Here d_{eff} is a quantity describing the strength of the second order nonlinearity of the materials, L is the phase-matched length of the nonlinear medium, ***I*** is the laser beam peak intensity, n_ω and n_{THz} are the optical and the THz group refraction index respectively. In order to generate THz output energy efficiently, a material with a high non-linear susceptibility d_{eff} (quadratic dependence) and an intense laser pulse are needed. The last term provides the general phase matching condition to ensure a rather long rectification conversion length. Due to the fact the optical group velocity is consistently larger than the group velocity of the THz propagation field (e.g. in the frequency band of 1-10 THz), it would be necessary to create a tilted wave-front for the strong-field optical laser beam inside the non-linear crystal, and the tilted angle of $\theta \approx \cos^{-1}(n_\omega / n_{THz})$ (where $n_\omega < n_{THz}$) is satisfied the phase-match condition across the entire thickness of the crystal, thus enhance the conversion efficiency significantly (as illustrated in Fig.5.10). The focused laser beam asso-

ciated with the extremely strong field e.g. 10^{17}W/cm^2 could be scaled up with THz pulses leading to the field strengths in the order of ~1 MV/cm.

Using the laser derived single-cycle THz pulse would make the diagnostic apparatus more compact, and also make it quite flexible to choose the location of the diagnostics, which could be in the X-ray transport tunnel after the undulator section or anywhere available downstream, close to or within the experimental hall. However, the laser pulse is apparently an external radiation source independent with the FEL SASE pulses, therefore the key element to realize this diagnostics would still be controlling and characterizing the temporal jitters between the optical laser pulses and the X-ray FEL pulses to improve the temporal resolution. A. L. Cavalier et al. developed the strong-field laser derived single-cycle THz pulse technique, and applied this technique to characterize the FEL pulses at both FLASH and LCLS. Currently this technique is proved working effectively for the photon energy of 100-1000 eV to achieve the single shot resolution. Most remarkably, it is claimed to work as both the FEL pulse arrival time monitor (for ~10 fs temporal resolution) and the FEL pulse temporal profile monitor (for <50 fs FWHM resolution) at the same time [25].

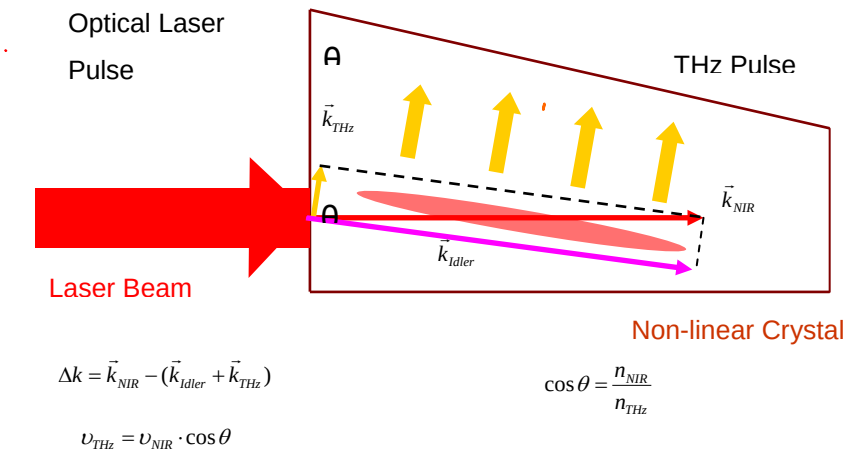

Fig.5.10 *the tilted wave-front of an optical laser pulse is applied to generate a THz pulse in a non-linear crystal (e.g. MgO-doped LiN_bO_3).*

5.1.3 Electron Bunch Streaking Technique

In order to measure the FEL X-ray pulse temporal profile, an indirect method to measure and characterize the electron bunch temporal distribution using a transverse RF beam deflector has also been extensively investigated at both LCLS and DESY (called LOLA project). Through accurate measuring and comparing the post-undulator bunch pulse transverse deflection (or streaking) signals for the lasing (FEL-on) and non-lasing (FEL-off) cases, the FEL X-ray pulse profile could be retrieved and reconstructed.

This technique was discussed by an internal electronic proceeding at SLAC [26]. The schematic layout of the diagnostic setup is given in Fig. 5.11. After exit from the undulator segments, the electron bunch pulse is delivered into an 'X-band' RF deflector and a dipole magnet sequentially. The RF deflector streaks the electron bunch in the transverse plane of the beam propagation direction, where the front and the tail of the bunch would experience the different deflection forces due to the ramping RF voltage, thus the spread of the electron deflection in one transverse coordination (horizontally as illustrated in Fig.5.11) could reflect the longitudinal profile of the bunch pulse. Then the bunch pulse enters into a dipole magnet, which applies an orthogonal (respect to the RF deflection force) Lorenz force to the bunch in the transverse plane (vertical axis in Fig.5.11). Thus the electrons possessing different kinetic energies would deflect different amounts in the vertical coordinate. The deflection signal of an electron bunch could be measured as a 2D profile in the transverse plane by a monitor screen located down-stream, and this signal directly maps the temporal profile and the electron kinetic energy distribution of the specific electron bunch pulse.

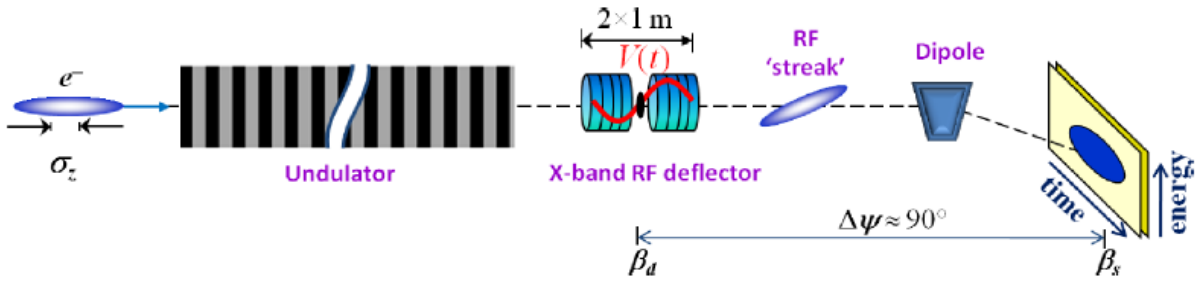

Fig.5.11 *a post undulator setup including a transverse RF deflector and a magnet electron energy spectrometer to measure the electron bunch temporal and energy profiles (from [26]).*

The working principle of transverse RF deflector for the electron beam temporal device is discussed in other references (e.g. [27]), where the X-band means the device is designed to work at the high frequency band of ~10 GHz. The RF deflecting force applies a transverse momentum to the bunch and the horizontal 'kick' is associated with a transform element of $R_{12} \cong (\beta_{xd}\beta_{xs})^{1/2}\sin(\Delta\psi)$. Where the Betatron of $\beta_{xd} \cong \sigma_{xd}^2/\varepsilon_{xd}$ or $\beta_{xs} \cong \sigma_{xs}^2/\varepsilon_{xs}$ is related to the transverse beam size and bunch charge geometric emittance in the 'x-coordinate' at the RF deflector (d) and the monitor screen (s) respectively; and $\Delta\psi$ is the phase shift of the horizontal Betatron from the RF deflector to the screen. The optimal RF phase is usually selected as the local maximum of Betatron β_{xd} at the deflector, and the local minimum of β_{xs} at the screen, which could give the best temporal resolution for the electron bunch pulse profile [27].

Then the transverse position of each relativistic electron on the screen is,

$$\Delta x(t) = \frac{eV_0}{pc}\sqrt{\beta_{xd}\beta_{xs}}\left|\sin\Delta\psi\right|\cdot\left(\frac{2\pi}{\lambda_{RF}}\cdot ct\cdot\cos\varphi+\sin\varphi\right) \quad (5.14).$$

Where V_0 is the deflecting voltage, p is the electron momentum, c is the velocity of light, λ_{RF} is the RF wavelength, and φ is the relative phase of the electron bunch within the RF signal cycle. It is quite obvious, the device operating at the zero-crossing phase $\varphi \approx 0$ would provide the optimal streaking effect and best temporal resolution, and the horizontal beam size on the screen is directly correlated to the electron bunch length $\sigma_x \propto c\cdot\sigma_t$. However when a non-zero-crossing phase is applied, there would be a offset from the horizontal centroid as: $\langle\Delta x\rangle_{off-set} \propto \sin\varphi$. At the near zero-crossing condition $\varphi \approx 0$, the Eq. (5.14) would lead to,

$$\sigma_x = \frac{eV_0}{pc}\sqrt{\beta_{xd}\beta_{xs}}\left|\sin\Delta\psi\right|\cdot\frac{2\pi}{\lambda_{RF}}\cdot c\cdot\sigma_t \quad (5.15).$$

By applying the parameters for LCLS hard X-ray beam (e-beam ~13.6 GeV and X-ray photon energy ~8 keV), the temporal calibration

factor $S = \sigma_x / c\sigma_t \approx 128$ could be obtained. And the temporal resolution of the deflector is calculated as $\sigma_{t,r} = \sigma_{x0} /(c \cdot S) \sim 2$ fs, which is claimed as the highest level of the temporal resolution among all kinds. The electron energy resolution associated with the dipole magnet could also be evaluated as well, which is determined by the kinetic energy of the electrons, and the geometry and the field strength of the magnet. However, this method can only resolve the temporal profile and energy spread of the relativistic electron bunch. In order to characterize the FEL photon pulse derived by the electron bunch pulse in the undulator, further procedures are required.

Concerning a nominal bunch charge mode of 250 pC with e-beam peak current of ~3 kA for the hard X-ray beam (electron kinetic energy of 13.6 GeV and radiation wavelength of 1.5 Å), the 2D deflection image of the electron bunch through the aforementioned diagnostic device (in Fig. 5.11) and projected at monitor screen could be simulated, where the 'x-axis' represents time and the 'y-axis' represents energy. At the 'FEL-off' case (Fig.5.12 (a)), the time-resolved e-beam energy and spread is recorded as a relatively narrow feature, corresponding to the collective signals from undulator spontaneous radiation, transverse deflection effect and coherent synchrotron radiation in the dipole etc. While the FEL is switched 'on', it would introduce an additional energy loss associated with a much broader energy spread across the overall bunch pulse due to the FEL radiation (Fig.5.12 (b)). The difference in-between the 'FEL-on' and 'FEL-off' images could be used to determine the electron kinetic energy loss or broadening $\Delta E_{FEL}(t)$ purely induced by the FEL radiation at the specific time-slice within the bunch length duration. In reality, the upper stream bunch compressor (e.g. the second bunch compressor within the LCLS Linac beam-line) already introduced a transverse kick to the electron bunch, which is tilted associated with its longitudinal phase. Since the reconstruction technique would mainly relay on the transverse streaking (or kick) by the RF deflector, so the compressor introduced bunch tilt need to be concerned and compensated. The effect can be well canceled by performing a second measurement at the adjacent zero-crossing of the RF cycle (180° phase shift from the first measurement). The reconstructed electron bunch peak current profile $I(t)$ by the two adjacent zero-crossing phases is given in Fig. 5.12 (c). Now the X-ray FEL power

temporal profile can be directly determined by $P(t) = \Delta E_{FEL}(t) \times I(t)$, and shown in Fig. 5.12 (d). According to the discussion in Chapter 3, the coherent time in a SASE process for the hard X-ray photon is around 100-200 atto-seconds. Thus due to the temporal resolution of the diagnostic device is ~2 fs, the fine individual coherent spike is smeared out and couldn't be resolved, and the reconstructed pulse profile in Fig.5.12 (d) only reflects a smoothed and averaged FEL power distribution.

In the meantime, the low bunch charge mode (e.g. ~20 pC) with shorter bunch duration or at the lower kinetic energy (e.g. ~4.3 GeV) for softer X-ray radiation (e.g. ~15 Å wavelength) could also be implemented to this FEL pulse reconstruct simulation scheme. The coherence time for the soft X-ray is much longer e.g. 1~2 fs, so the technique could in principle resolve the single coherent spike in a SASE FEL pulse in the soft X-ray range. Apparently the electron bunch streaking technique along with the electron energy spectrometer provide very high temporal and energy resolution, which could be used to reconstruct the FEL pulse. It is a very promising method to measure the short wave pulse profile and is currently in the development at LCLS and planned to be commissioned in 2013. However the diagnostic setup is quite complicated and the measurement is also not easy in practice. Especially this is an indirect method, and the X-ray pulse could only be derived and reconstructed through measuring the instantaneous electron energy loss of the bunch charge in its longitudinal phase.

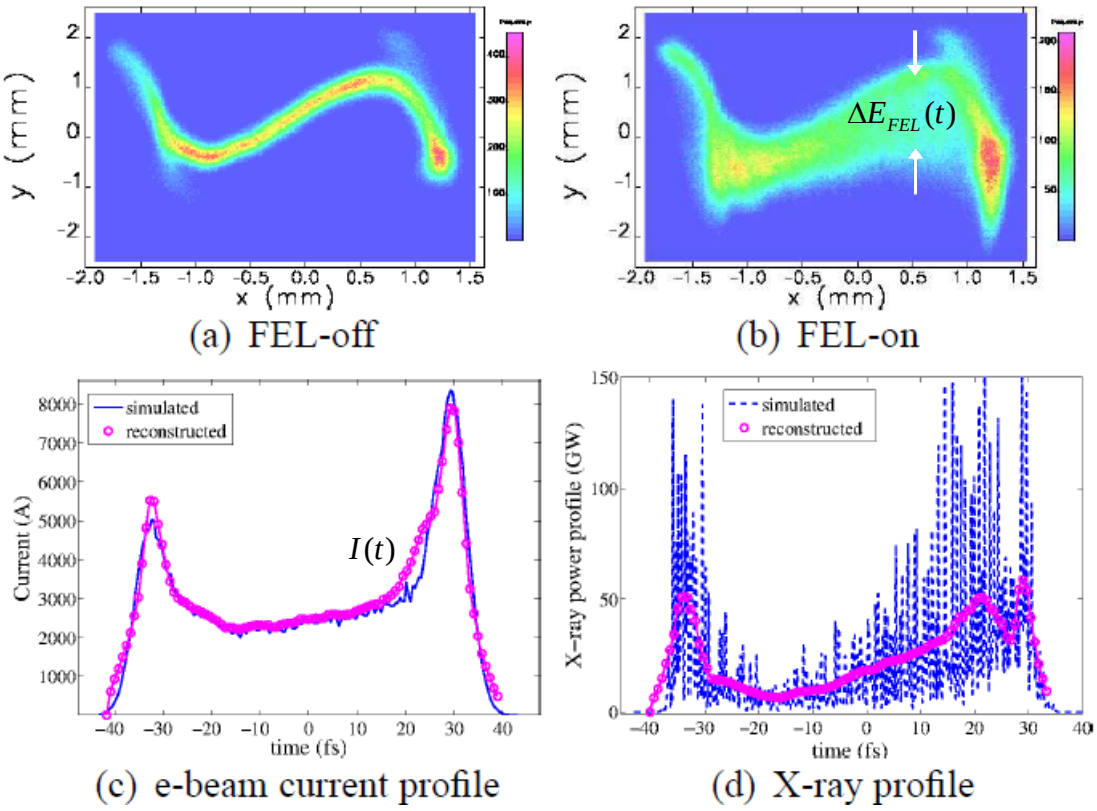

Fig.5.12 *The simulated images at the monitor screen representing e-beam (kinetic energy 13.6 GeV, bunch charge 250 pC) longitudinal phase and energy distribution for the case of (a) FEL-off and (b) FEL-on. (c) and (d) show the reconstructed e-beam current and FEL X-ray profiles comparing with the simulated signals for the non-lasing and lasing cases respectively (from [26]).*

Here we just enumerated and discussed a few methods which could be potentially used for measuring and characterizing the X-ray photon pulse duration and the pulse temporal structures for the European XFEL. Apparently there are limits and technical challenging for each of these techniques. Further investigation and development are still on-going to verify their applications, reliability and limits etc. for the practical diagnostics. Moreover, the spectroscopic characterization of X-ray is also an in-direct approach, which is actually corresponding to the Fourier transformation of SASE pulse temporal profiles. This would require the development of the high-energy resolution X-ray spectrometer covering from the soft X-ray to the hard X-ray range [28].

5.2 X-ray Photon Pulse Arrival Monitor

X-ray pump-probe measurement is a cross-correlation method where an X-ray pulse induced the perturbation to a system within the ultrafast time-scale while another external short radiation pulse is set to arrive at various time delays to monitor and characterize the ultrafast changes of the system in real time. The external radiation source could be a visible or NIR laser pulse, a long wavelength radiation pulse (e.g. THz), or the HHG atto-second pulse of an optical laser etc. The pump-probe scheme could also be arranged in vice-vitae, where the external radiation pulse acts as the 'Pump' and the X-ray FEL pulse is the 'Probe'. Therefore the accurate measurement for the delay time in-between the X-ray FEL and the external radiation pulses, and monitoring of their mutual temporal jitter distribution at the shot-to-shot basis would be essentially important for the X-ray pump-probe experiment. And the X-ray pulse arrival monitor is a non-disregarded photon diagnostics for the X-ray Free Electron Laser System.

5.2.1 Spatial Encoding & Single-Shot Imaging Technique

X-ray pulse induced ultrafast transient changes of the optical reflectivity in the materials can be used as an effective tool for charactering the X-ray/visible laser pulses cross-correlation. The synchronization between the X-ray FEL pulses and the external optical laser pulses can be realized through the radio-frequency (RF) master oscillator locking technique developed and commissioned at the FLASH successfully, where the RF signals of the injector/booster for the electron bunches used to accelerate in the LINAC and to drive the X-ray pulse radiation in the undulators are synchronized with the pulses of an external femtosecond laser oscillator (which could be the seed of the further amplified laser pulses for the user experiment) through fine tuning its optical cavity length and the phase shift of the cavity mode. Eventually the user optical laser pulses and the X-ray FEL pulse train are locked through this so-called "Phase Locked Loop" (PLL). Due to the instability/fluctuation of the FEL accelerator electronic sub-systems, and the large scale of the synchronization & timing distribution system, the shot-to-shot temporal jitter of the pump and probe pulses is in the range of a few hundred femto-seconds.

Measuring and monitoring of the aforementioned shot-to-shot temporal jitter distribution is in great demand for the X-ray pump and probe experiment, especially for those targeting for single-shot measurement and resolution. The X-ray pulse induced transient change of the optical reflectivity is one of the most typical and effective methods developed for this purpose, and it mainly includes two major categories. One is called the averaged signal scanning method used to measure and calibrate the X-ray induced dynamic features at each setting delay, and the other is implementing the same principle but through the single-shot imaging method to characterize the pump-probe delay for the single shot data. The scanning method was initially developed by C. Gahl et al. using the EUV light of ~40 nm wavelength at FLASH [29], was then further developed by W. F. Schlotter et al. at LCLS to the soft X-ray range up to 2 keV [30].

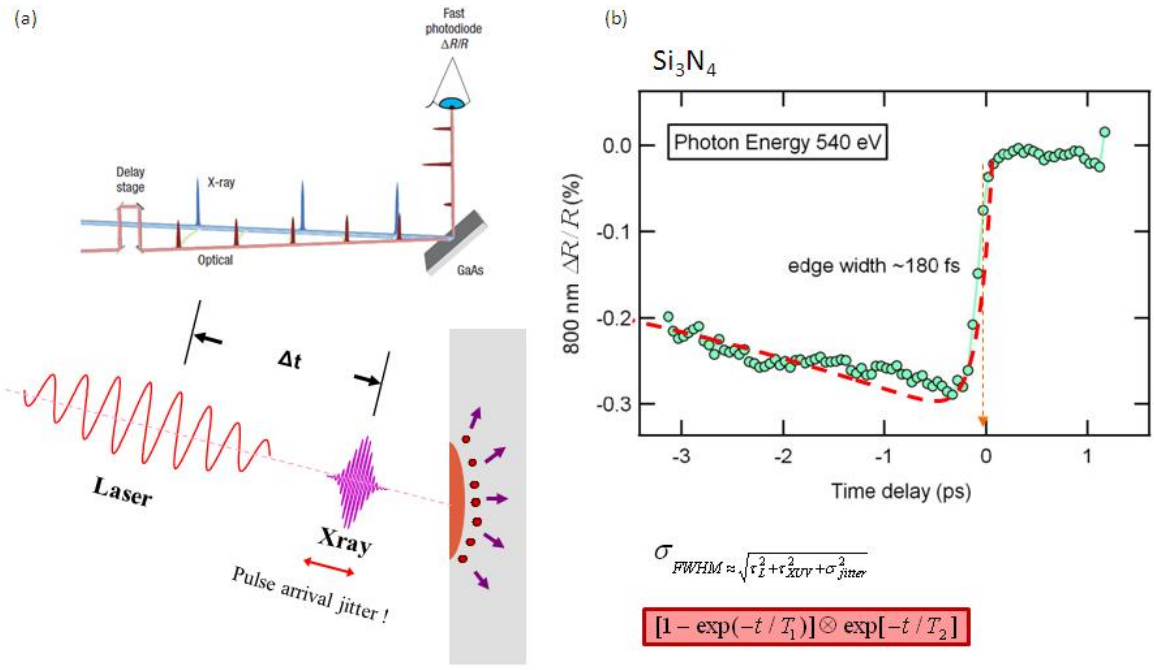

Fig. 5.13 *(a) The typical layout of the X-ray induced transient change of the optical reflectivity (ΔR/R) measurement (from [29]). (b) The typical signal of the transient change of the optical reflectivity at the photon energy of 540 eV on a Si_3N_4 surface (private communication, from [42]).*

The average scanning delay method of the surface transient reflectivity measurement is depicted schematically in Fig. 5.13 (a), where the X-ray FEL beam and the optical beam incident co-linearly (or with a small crossing

angle) on a semiconductor sample surface (e.g. Si_3N_4 or GaAs), and the X-ray and the optical pulses are phase-locked through the PPL electronics introduced previously, either having the same repetition rate or letting the repetition rate of the optical laser is n times of that of X-ray FEL. The transient change of the optical reflectivity at various delays induced by the FEL pulses is measured by a photo-diode, where the relative change of the optical reflectivity could be referenced and calibrated by the un-pumped signal, and normalized by the X-ray pulse energy and intensity under the shot-by-shot base. The fundamental setup for this type of X-ray/optical cross-correlator also includes an unpolished scintillation screen (e.g. Ce:YAG crystal) used to monitor the spatial overlapping between the optical laser beam and the X-ray beam, and a semi-rigid SMA coaxial cable connected antenna used for searching the coarse delay zero. The X-ray or the optical laser pulse could induce a fast photoemission current signal in the feedback circuit, which could be sent to an oscilloscope through a broadband input coupling (e.g. > 40 GHz) which guarantees that the temporal resolution of the coarse timing device is better than 25 pico-seconds. A practical routine at LCLS could improve this coarse timing resolution to about 4 ps time scale. The fine femto-second cross-correlation is realized through the aforementioned transient reflectivity measurement setup, where a photo-diode or a photo-multiplier is set at the reflection angle of the optical light to measure the optical reflectivity from the surface. The X-ray FEL and other stray lights are filtered out using an optical filter, and the various delays are generated through a delay stage within the optical laser beam line. The pulse energies of both the optical light and the X-ray are measured and recorded respected to each individual timing stamp as their identification.

According to the results reported in Fig. 5.13 (b) [30], the X-ray FEL pulse induced transient changes of the optical reflectivity $\Delta R/R$ spans the timescales from a few tens of femtoseconds to a few hundred picoseconds. The initial ultrafast step edge near the delay “zero” in the transient optical reflectivity change upon the intense X-ray radiation is our major interest, where the time scale for this sharp edge is actually corresponding to the convolution of the optical laser pulse and an exponential decay function which can reflect the X-ray pulse induced transient free electron carriers build-up and de-excitation processes in the conduction band of the semiconductor

sample, and the incorporation of the delay time jitter of the X-ray and optical laser pulses. As plot in Fig. 5.13 (b), the temporal feature of the transient signal could be fitted by a convolution function of,

$$\propto [1-\exp(-t/T_1)] \otimes \exp(-t/T_2) \quad (5.16).$$

Where T_1 and T_2 indicate the onset time and the decay time of the signal of the free carriers in the semiconductor respectively, and the energy of these free carriers are within a few eV above the Fermi level of the sample. According to the Drude model, the present of these free carriers close to the Fermi level caused the significant change to the refraction index (near the visible light range) of the sample, which could be displayed as the change of the optical reflectivity. As already mentioned previously, this method would be suffered by the shot-by-shot pulse intensity fluctuation of both the X-ray and the optical laser, and by the temporal jitter of the delay of X-ray/optical laser pulses (including the X-ray pulse arrival jitter, which is mainly associated with the electron bunch arrival time in the undulator of the X-ray FEL beam line; and the optical laser pulse arrival jitter, which is mainly determined by the laser oscillator instability/phase shift, the temporal fluctuation of various optical laser pulse amplification stages, and as well as the electronic fluctuation associated with the timing distribution system including the short or long term change of the ambient environment). Therefore the delay-scanning measurement won't work at the single shot basis for each delay setting, it will work only if the measurement satisfies a certain level of statistics, which means only the average signals (of a large number of the single-shot measurements) at various time delays can achieve a discernible S/N ratio and resolvable transient phenomena. According to [29], if the optical laser pulse of ~10 nJ energy is used as the probe, a number of ~20,000 pulses are needed to smooth the time-resolved signals in the transient reflectivity curve. The typical X-ray FEL parameters for the surface transient reflectivity measurement are: i) ~10 μJ pulse energy, ii) a few tens of fs pulse duration, iii) beam diameter of 200~300 μm, iv) the incidence angle to the sample could be an arbitrary angle (e.g. ~45˚) or the surface normal. Generally the ideal FEL beam intensity should be around ~10 mJ*cm^{-2}, big enough to induced sufficient amount of transient free carriers in the sample, but well below the damage threshold. For the optical probe beam, the intensity is usually one or two order smaller; a sub-μJ pulse should provide the desirable energy, which

can only cause a minor/negligible influence to the sample surface compared to the pump.

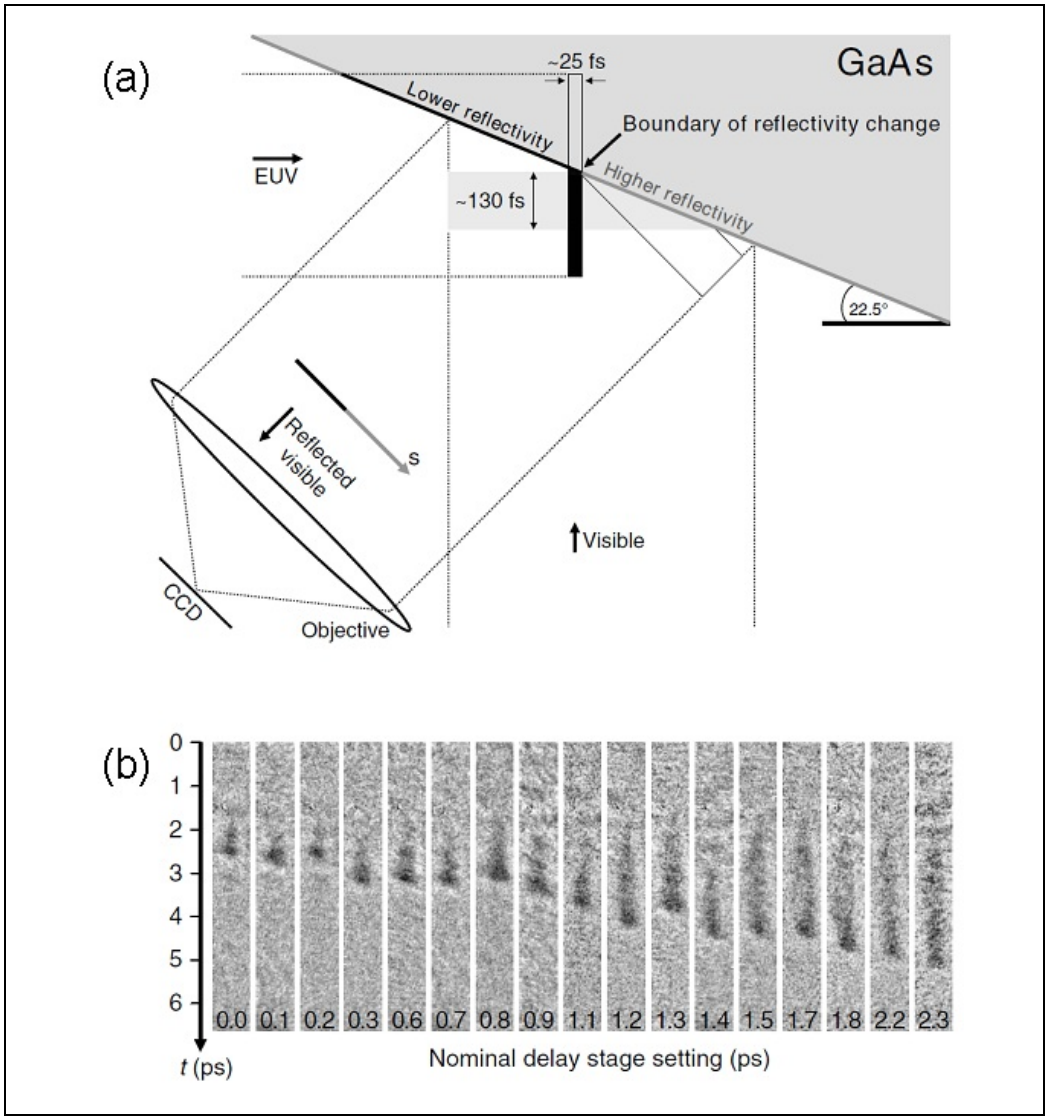

Fig. 5.14 *(a) The layout of the single-shot imaging pump-probe experiment. The XUV beam comes as the orthogonal direction to that of the visible light, the two beams cross each other through a semi-conductor sample surface. The XUV pulse is absorbed by the surface and changes the reflectivity for the visible pulse. The optical pulse is reflected off the sample surface at 45°, and the image is recorded by a CCD camera. (b) A series of single shot CCD images taken by the setup in (a) are plot, where the cutting edge in each image indicates the nominal timing "zero" crossing of the two beams' wavefront. From [31].*

The single shot imaging method for charactering the temporal jitter between the X-ray and optical laser pulses was originally developed by Drescher and

co-workers at FLASH using the XUV pulses with photon energy of around 90 eV. The experimental details are illustrated and discussed in Fig. 5.14 [31, 32], in which the single shot imaging is recorded while the X-ray pulse and optical laser pulse are overlapping both in space and in time, representing the “real-time” temporal jitter distribution of the ‘pump’ (X-ray FEL pulses) and ‘probe’ (optical laser pulses) experiment, or the vice vitae. A series of single shot CCD images were taken in Fig. 5.14 (b), where the outstanding step edge in each image indicates the nominal timing delay “zero” crossing of the wave-packets of the two beams. However according to this work, the sharp step-edge in each single shot image spans the time-scale of >100 fs which indicates that the temporal resolution is not adequate. And the ideal X-ray pulse arrival diagnostics should have the temporal resolution down to a few tens of femtoseconds and eventually to achieve the temporal resolution of < 10 fs, and should be effective to much shorter waves e.g. the photon energy of a few keV.

Further investigation of the single shot imaging method for X-ray pump-probe experiment temporal jitter characterization is currently conducted at the LCLS SXR instrument [30, 33], targeting to achieve a better temporal resolution for the single shot pump-probe measurement, and to explore this technique into the soft X-ray range (from 500 eV to 2 keV), where various X-ray beam intensities, photon energies and different experimental conditions are applied and systematically investigated. Fig. 5.15 (a) gives the typical experimental apparatus at the SXR end-station for this type of the temporal jitter measurement through the single shot imaging. The X-ray FEL and the optical laser beams are overlapping at the surface of a Si_3N_4 thin film sit in the center of an experimental vacuum chamber. The X-ray beam incidents perpendicularly onto the Si_3N_4 surface, while the optical laser beam is sent to the surface with an angle of α ~45 deg. through a $\lambda/2$ waveplate, therefore the linear polarization of the optical laser could be mapped to an arbitrary angle within the transverse plane of the beam propagation. The transmission image (recorded by Camera 0) and the polarization resolved reflection images (recorded by Camera 1 or 2, and the s-polarized and p-polarized components are split by a polarized beam-splitter cube in the reflection beam path) are taken simultaneously to reflect the interaction of X-ray and optical laser at the surface and the X-ray pulse arrival times. Fig.5.15 (b) shows a typical single-

shot contrast image of the optical laser pulse upon the X-ray pulse irradiation, generated via the normalization of the raw image by the background image (where only the optical laser is applied while the X-ray beam was blocked). The value associated with each pixel of CCD camera for the single-shot image is divided by that of the background image, the big circle in the plot indicates the beam size of the optical laser, and the red contrast zone located close to the center of the optical laser spot indicates the region where the X-ray and the optical laser beams overlap and interact. The horizontal coordinate is corresponding to the time axis for the temporal overlapping and the relative delay of the two beam pulses, where the delay change Δt is associated with the displacement of Δx in this direction as (c is the speed of the light, and α is the optical light incident angle to the surface),

$$\Delta t = \Delta x \cdot \cos\alpha / c \qquad (5.17)$$

The vertical integration of the contrast image in-between the two dashed lines indicated in Fig. 5.15 (b) will result a one-dimensional line-profile, which could reflect the dynamical features of the free carriers in the Si_3N_4 thin film upon the X-ray pulse irradiation, apparently in-corporated with the X-ray beam transverse profile as well as the pulse duration of the optical laser. Fig.5.15 (c) displays the layout of the line-profiles (generated by the integration method discussed above) from many single shots (>1000 shots) within a same experimental run, where the experimental conditions were supposed to maintain the same. Various colored vertical lines are denoted in the plot, among them the contrast step edge in the middle section of the plot (associated with the horizontal pixel indexes in-between 500 and 600) in principle reflects the nominal timing delay “zero” crossing of the X-ray and the optical laser wave-fronts. Measuring and calibrating this step edge for each individual single shot, is the general method to characterize the temporal jitter distribution in-between the X-ray and the optical laser pulses for the X-ray pump-probe measurement. Fig.5.15 (d) only highlights a single 1D line profile selected from the whole array of the linear elements in (c). The high contrast and sharp step edge in the plot displays that the single-shot imaging method we developed at LCLS could achieve sub-20 fs temporal resolution as long as the appropriate X-ray beam intensities are applied. Further investigation by fine tuning the X-ray beam intensity also shows the high temporal resolution

could be well maintained for a few orders of dynamics range (data in analysis and not shown).

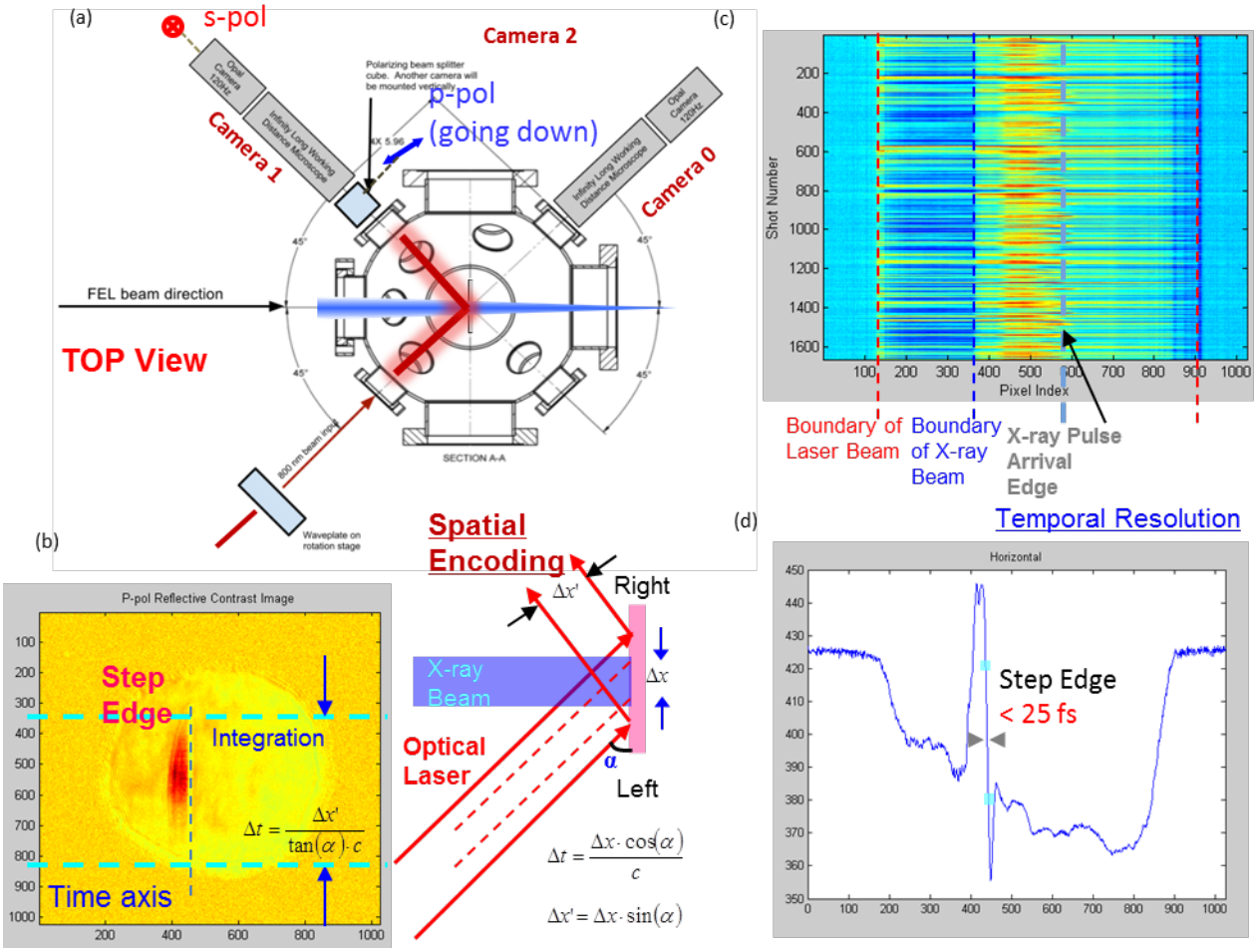

Fig. 5.15 *(a) the top view of the LCLS SXR experimental end-station, along with the layout of the X-ray FEL and the optical laser beams. The two beams are overlapping at the surface of a Si_3N_4 thin film (in sub-micron thickness) located at the center of the chamber, the transmissive image and the polarization resolved reflective images are taken simultaneously to reflect the interaction of the X-ray and optical laser and their mutual arrival time (private communication, from [30]). (b) The plot is a typical contrast image (explained in the text), where the big circle indicates the beam size of the optical laser, and the red contrast zone indicates the interaction of the X-ray with the optical laser. (c) The contrast imaging integrated line-profiles (explained in the text) of many single shot images for an experimental run. (d) The X-ray pulse arrival time calibration through measuring the location of the step edge in each single shot contrast image line-profile, which demonstrates achieving the temporal resolution of < 25 fs is feasible (unpublished results).*

Fig. 5.16 (a) shows the most recent result from an in-house research campaign at the LCLS SXR instrument, where the temporal jitter distribution (i.e. the X-ray pulse arrival times respected to the arrival times of the optical laser) of >8000 single shots in an experiment run is plot. The connection in-between Fig.5.16 (a) and Fig.5.15 (c) is actually Eq. 5.17, where the displacements of the step edge Δx in the single shot images are corresponding to the different mutual delays of the X-ray and optical laser pulses Δt, that is also why this technique is named as the spatial encoding. The measurement demonstrates that the short term (e.g. for 1 or 2 minutes) temporal jitter distribution for the X-ray pulse arrive times of the LCLS is around 200-300 fs. This is more clearly displayed in Fig. 5.16 (b) by the histogram of (a), where a full width half maximum (WFHM) of ~250 fs jitter distribution is obtained. Our research carried at the SXR end-station was mainly focused on investigating the XUV to soft X-ray wave (i.e. the photon energy of 500 eV to 2 keV) induced transient change of the optical reflectivity, and utilized the proper thin-foiled and light-transparent materials to develop the photon pulse arrival monitors. Due to the restriction of the photon energy at SXR is below 2keV, the hard X-ray beam induced transient reflectivity changes have not yet been studied by our group, however another team has already looked into this and observed promising results at XPP [34]. Developing the hard X-ray photon temporal diagnostics is a general interest to the hard X-ray beam lines of LCLS and SACLA at this moment, and eventually to the SASE1-2 beam-lines of the European XFEL. A hard X-ray photon has much higher photon energy compared to that of the soft X-ray photon, therefore the absorption of a hard X-ray photon could induce much higher free carrier density and larger non-linear dynamics across the sample. However the photo-absorption cross-section for the hard X-ray is relatively smaller for most of the commonly applied materials (especially the low-Z materials), corresponding to a much longer attenuation length. So the hard Xray induced transient influence would distribute not only within the surface portion, but also down to the deep bulk. Then upon the X-ray irradiation, the optical transmissive image is expected to have a higher contrast compared to the reflective image. Then the elements or compounds with relatively higher-Z could also be proposed for the hard X-ray diagnostics, to enhance the signal level of the transient change of the optical reflectivity at the surface, but obviously this would cause more attenuation and deviation to the beam.

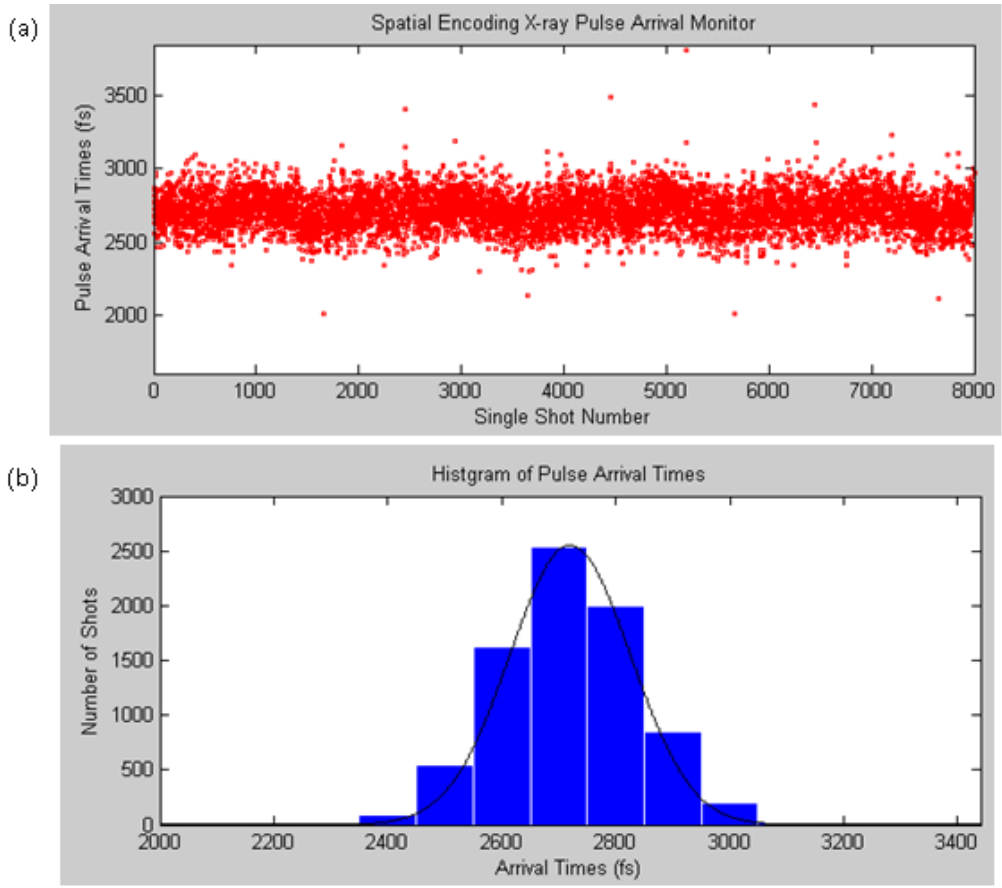

Fig. 5.16 *(a) a recent in-house beam experimental campaign at the LCLS SXR instrument to characterize the X-ray pulse arrival times (including ~8000 single shots in an experimental run). (b) The Histogram of the X-ray pulse arrival time distribution in (a), reflects the short term temporal jitter distribution of LCLS is about 250 fs FWHM (unpublished results).*

5.2.2 Spectral Encoding Technique

Another approach for characterizing the delay time in-between the X-ray/optical pulses through measuring the X-ray pulse induced transient change of the optical reflectivity is utilizing the 'spectral encoding' method in an chirped optical laser pulse [35]. Compared to the spatial encoding technique where the temporal delay information is encoded as the relative displacement in the transverse plane of the X-ray beam propagation direction (as discussed previously), the spectral encoding method determines the delay or X-ray pulse arrival time through characterization of the spectral modulation at the specific wavelength in the spectrum of the chirped optical pulse.

The layout of a spectral encoding setup along with its principle is sketched in Fig.5.17. It is a modified version from the original set-up discussed in [35]. Here a standard optical pulse stretcher is used to stretch the ultrafast Ti:Sapphire laser pulses to the picosecond pulses. A Ti:Sapphire laser oscillator emitting a broadband spectrum of 750-850 nm, can delivery ultrafast pulses of < 20 fs duration. The optical stretcher is typically used in the chirp pulse laser amplifier to stretch the ultra-short laser pulse to the pulse duration from a few up to a few hundred pico-seconds, mainly determined by the geometry and orientation of the diffractive optics inside the stretcher. Then through certain amplification scheme, the stretched chirp pulse could be amplified to the magnitude of several orders higher, usually corresponding to the optical laser pulse energy of a few or a few tens of mJ. Here only the pulse stretching technique and the generated chirp pulse before compression are used in the proposed diagnostics.

As illustrated in Fig. 5.17, the chirp pulse is created having positive group velocity dispersion (GVD), where the redder waves travel faster compared to the bluer ones, thus encoded as the front of the laser wave-packet. The chirped laser pulses could be well synchronized with the X-ray FEL pulses and co-lineally overlapping with them in a thin film of Si_3Ni_4 with thickness of 500 nm (only a fraction of one optical cycle of the Ti:Sapphire laser with central wavelength at ~800 nm). Upon transmission through the Si_3Ni_4 thin-film, the optical laser beam is reflected off a thin Aluminum film with sub-micron thickness and then sent into an optical spectrometer, while the X-ray beam could penetrate the Al-thin film with only a mild attenuation (the attenuation length of Si_3N_4 for the X-ray photon at >2 keV is larger than 2 μm). Thus this device is working as an on-line non-invasive X-ray pulse arrival monitor. If assuming the stretcher provides an approximate linear chirp to the whole spectrum of 750-850 nm and stretches the optical pulse length to 5 pico-seconds, then the chirp of the optical laser pulse is ~50 fs/nm.

The optical laser beam diffracts by a grating insider the optical spectrometer. Using the grating equation: $d \cdot (\sin\alpha + \sin\theta_m) = m \cdot \lambda$, where m is the diffraction order of the grating, d is the groove spacing, α is the beam incident angle to the grating surface normal, θ_m is the diffraction angle of the m-th order, it is easy to derive the angular distribution of the wavelength diffraction

for the first order of a collimated optical beam is $\frac{\Delta\theta}{\Delta\lambda} = \frac{1}{d \cdot \cos\theta}$. If a spherical mirror of radius of R is used in the spectrometer (in Fig.5.17), then the spectral line-width distribution at the CCD detector located on the focal plane of the spherical mirror is $\Delta x \approx \frac{R}{2} \cdot \Delta\theta = \frac{R}{2d\cos\theta}\Delta\lambda$. If the grating groove density is1000ln/mm, R = 200mm, the incidental beam comes as the grating normal ($\alpha \approx 0$), and with implementation of linear chirp pulse $\frac{\Delta t}{\Delta\lambda} \approx \frac{50\,fs}{nm}$, it could derive the time delay correlated to the transverse displacements (encoded as the various wavelengths of a chirp pulse spectrum) in the CCD camera is:

$$\Delta t \approx 300\,fs \cdot (\Delta x[mm])$$

If the best spatial resolution of the CCD chip is ~50 μm (corresponding the size of a few pixels), the step-edge in the contrast image indicating the X-ray pulse induced the transient change of the optical reflectivity of the sample could be resolved at this length scale, which means the optimal temporal resolution of using such a chirp pulse spectral encoding technique could be as good as ~15 fs. And all the imaging process/analysis schemes we developed for the spatial encoding technique are still effective and could in principle be applied and used to the spectral encoding technique.

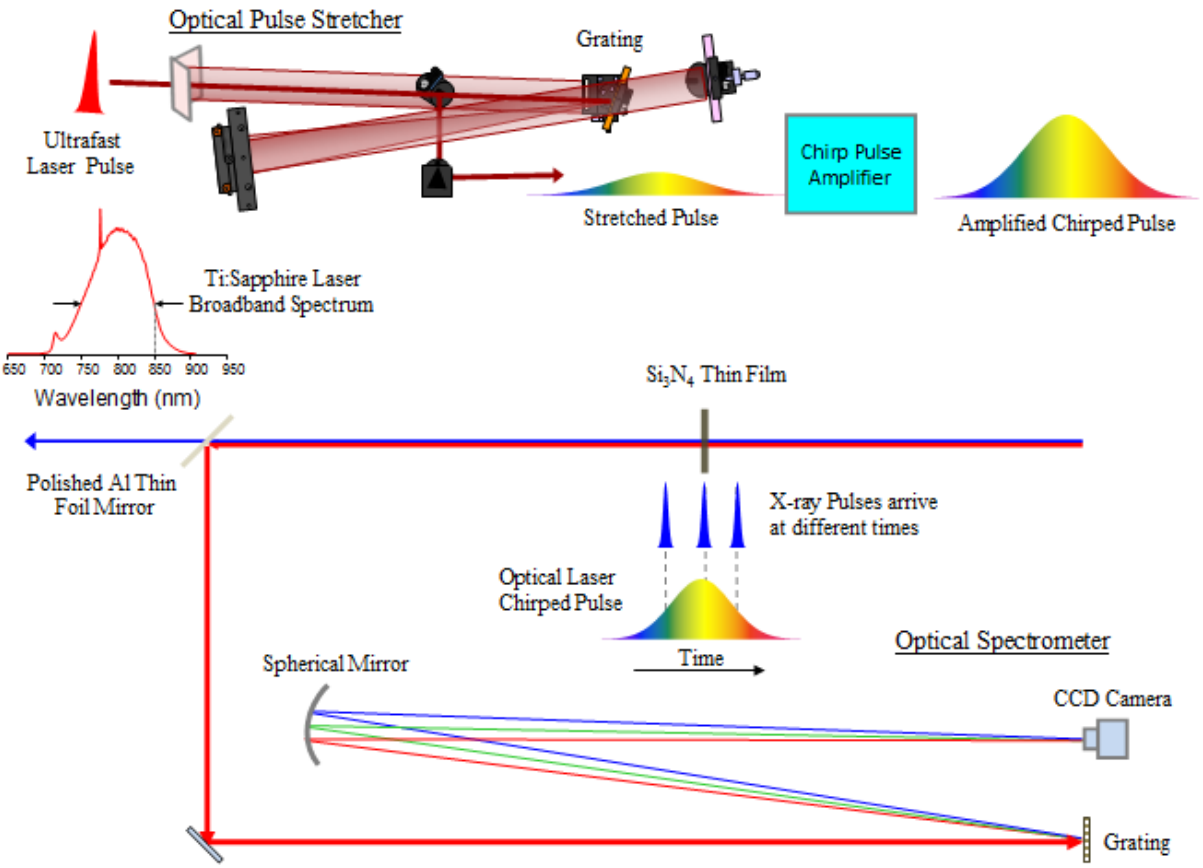

Fig. 5.17 *Ti:Sapphire Laser chirped pulses overlap with the X-ray FEL pulses within a Si_3N_4 thin film, the X-ray pulse induced transient change of the optical reflectivity is encoded in the chirp pulse laser spectrum, reflecting the various X-ray pulse arrival times relevant to the optical laser pulses.*

5.2.3 Parasitic Edge Radiation Technique

When the saturated, high beam intensity and high peak brilliance SASE pulse is created in the undulator of a FEL facility, a permanent bending magnet located at the lower stream of the last undulator segment is applied to separate the FEL radiation pulse from the electron bunch, working as the “beam dump”. The longitudinal velocity of the electrons would experience an abrupt change when they exit from the undulator and enter into the beam dump, producing a long wavelength edge radiation. Since this edge radiation pulse is generated by the same electron bunch which created the FEL pulse in the undulator, therefore it always has relatively fixed and stable phase compared to the FEL pulse, --- they are mutually “coherent”. According to the simulation by considering a virtual radiation source in the middle of the straight section in-between the undulator and the beam dump [36, 37], the

edge radiation field could be expressed as a function of the radiation frequency ω and the transverse coordinate r,

$$E_{ER}(\vec{r},\omega,t)=\frac{\vec{e}_r(-e)\cdot 2\omega}{4\pi\varepsilon_0\cdot cL}\left[\int_{-\infty}^{\infty}d\tau\left[\sin c\left(\frac{\omega\cdot r^2}{cL}-\omega\tau\right)-\sin c\left(-\frac{\omega\cdot r^2}{cL}-\omega\tau\right)\right]f(t-\tau)\right] \quad (5.18).$$

Where L is the length of the straight section (i.e. the distance from the end of the undulator to the beam dump), and $f(t)$ is the electron bunch longitudinal density distribution function. The averaged edge radiation field could be obtained by the integration of the Eq. (5.18) in the radial coordinate up to the transverse beam size σ,

$$E_{ER}(t)=\int_0^{\sigma}d\vec{r}\cdot E_{ER}(\vec{r},\omega,t)/r \quad (5.19)$$

Applying the experimental conditions at FLASH: the electron kinetic energy of 580 MeV, the straight section length L of 12 m, and the cut-off frequency of ZnTe (since a ZnTe crystal is used as the diagnostic sample for the experiment, then the cut-off frequency for the electro-optic effect of ZnTe should be applied, thus the response frequency $\omega\le\omega_c$ ≈ 2.5 THz), the peak of the calculated edge radiation field distribution is actually within the THz spectral range, which agrees pretty well with the experiment. Both the experimental measurement and the simulation results are plotted and compared in Fig. 5.18.

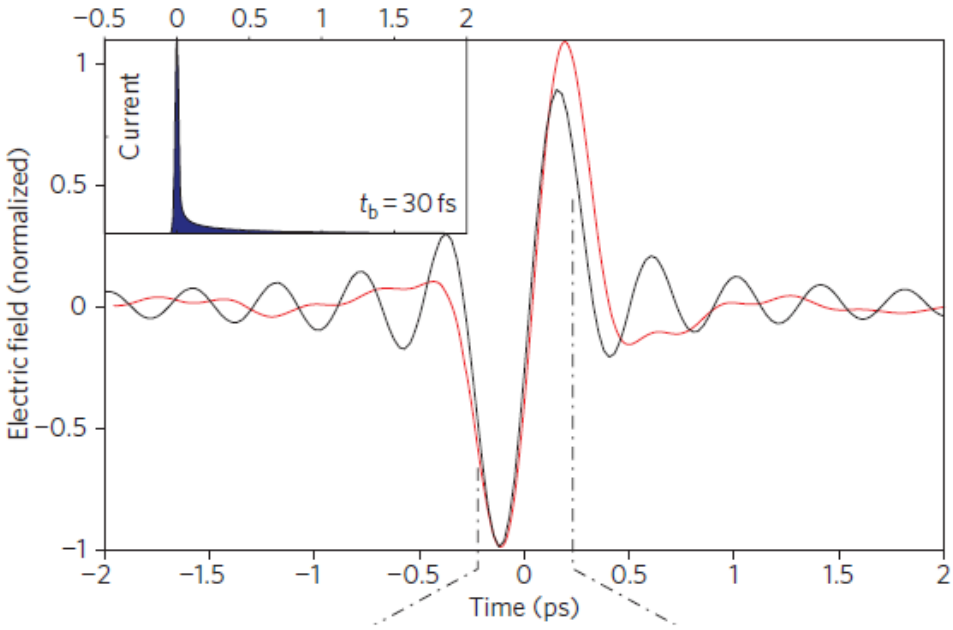

Fig. 5.18 *the electric field of the edge radiation pulse at FLASH, including both of the measured (red) and calculated (black) results (from [37]).*

F. Tavella et al. initiated a research campaign at FLASH to investigate the properties of the edge radiation, and explored its potential application for a parasitic on-line diagnostics. The principal layout of the experiment is given in Fig. 5.19. As discussed previously, a same electron bunch is used to create the X-ray FEL pulse in the undulator and the edge radiation pulse at the exit, therefore the mutual temporal jitters in-between the two pulses are very small and negligible compared to the other sources of the temporal jitter. Then measuring and characterizing of the temporal jitter in-between the edge radiation pulse and the user optical laser pulse could pretty much reflect the temporal jitter of the X-ray pump-probe experiment.

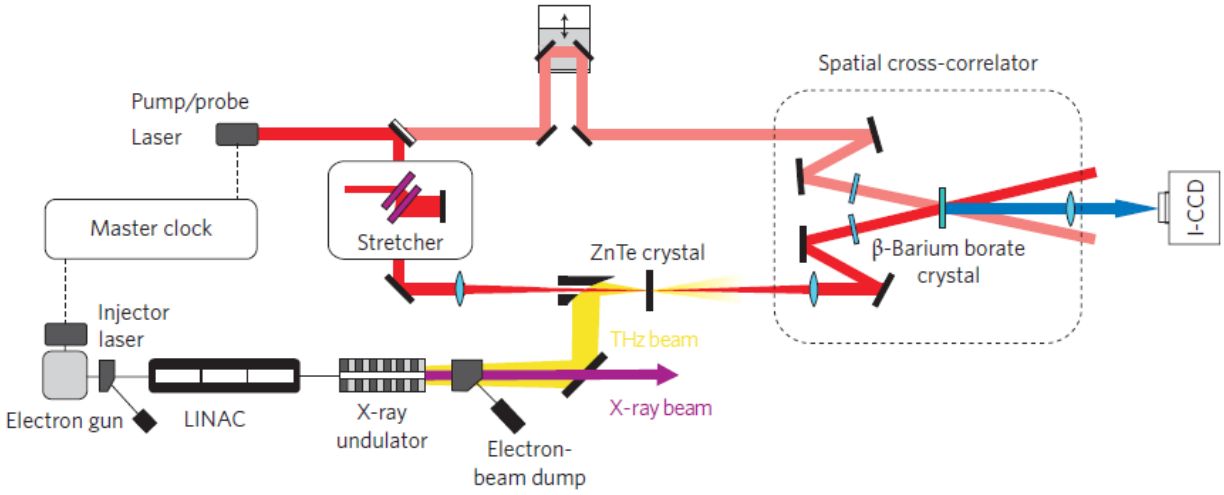

Fig. 5.19 *The schematic layout of the edge radiation cross-correlation setup at FLASH (from [37]).*

As illustrated in Fig.5.19, the user ultrafast optical laser beam was split into two components, one is sent to a delay generation line, and the other is sent through an optical pulse stretcher to create a chirped pulse. The edge radiation THz beam is focused down to enhance its field strength and overlapping with the optical chirp pulse at a thin ZnTe crystal, where the chirped pulse picks up the electro-optic effect induced by the edge radiation pulse $E_{ER}(t)$, and encode it to a specific wavelength in its broadband spectrum determined by the mutual arrival times of the FEL pulse (i.e. the edge radiation pulse) with respect to the optical laser pulse. Eventually the optical chirp pulse (with wavelength encoding) and the ultrafast laser pulse are crossing non-collinearly and frequency doubled in a non-linear crystal (e.g. BBO crystal). As in Fig.5.19, the relative wavefront tilt produces a mutual spatial-temporal delay in the frequency-doubled signal (SHG), whose wavelength dependent temporal intensity profile could be detected by a linear CCD chip, then relayed to an oscilloscope and displayed as an intensity cross-correlation trace. The signal on the scope (slow signal) could be calibrated through scanning the delay, representing the real cross-correlation signal (ultrafast signal) in-between the chirped and un-chirped optical pulses. The shift of the cross-correlation trace on the scope could directly reflect the change of the mutual delay in-between the FEL pulse and the user optical laser pulse.

This method is also using the spectral encoding technique, where the edge radiation THz pulse induced transient modulation was encoded into a chirped optical pulse to reflect the mutual arrival times in-between the FEL and the optical laser pulses. However the THz pulse is associated with a slow ramping electric field, corresponding to the time scale of >100 fs for an optical cycle. But referring to the precise fitting procedure, the accuracy of determining the mutual arrival times of the pump-probe pulses by using this technique is claimed to be better than 10 fs [37].

Now let's assess the differences of the European XFEL compared to the FLASH. Due to the fact that the European XFEL is the hard X-ray FEL facility mainly, the electron kinetic energy is much larger (>10 GeV) compared to FLASH (< 1 GeV). Providing the similar edge radiation setup and geometry are applied, the edge radiation spectral peak should thus shift into much shorter waves, e.g. into the near infrared, visible or even shorter wavelength ranges. And the condition $\varphi = 2\pi L/(\gamma^2 \cdot \lambda_{ER}) << 1$ is obviously much easier to be satisfied, which also indicates the edge radiation at the higher electron kinetic energy circumstance could be transported to a much larger distance over the straight section in-between the undulator and the beam dump. The advantage of using shorter wave over the longer wave is mainly because it is associated with a smaller beam radiation divergence and therefore the effective Rayleigh range is substantially larger,

$$z_R = \frac{\pi \cdot w_0^2}{\lambda} \qquad (5.20)$$ [38].

However the THz response of the ZnTe crystal might not be valid any longer, the diagnostic sample material would need to be changed. However the ideal candidates could still be selected from a broad range of conventional semiconductors or dielectrics, which have substantially transient electro-optical effect close to the visible light (or IR) spectral range.

5.2.4 Photoemission Spectral Sideband Technique

Previously the THz streaking technique used to characterize the X-ray photon pulse length and temporal profile is discussed (refer to Section 5.12), where since the condition of $\tau_X << T_{THz}/2$ is satisfied, the X-ray pulse induced ultra-short electron wave-packet is treated classically as within a slow changing electric field. Whenever the X-ray pulse length is extremely short (e.g. the sub-femtosecond FEL pulse from the low bunch charge mode, or the atto-second HHG pulse etc.), the streaking technique could be realized by using much shorter radiation wavelengths too (e.g. the optical laser pulse in the visible spectral range). However when a relatively longer X-ray photon pulse is used for the experiment (e.g. $\tau_X >= T_L/2$, similarly T_L is the optical cycle of the laser pulse applied to the streaking experiment), the classical treatment for the streaking technique is no longer valid, instead an alternative phenomenon – so called photoemission sideband would become overwhelmed [39, 40].

The typical experimental layout for the photoemission sideband measurement is illustrated in Fig. 5.20 (a), where the X-ray pulse (e.g. the FLASH XUV pulse with photon energy of ~92 eV) induces the photoemission from a Xe gas target, and the highest kinetic energy is associated with the electron emitted from the valence band. In the meantime, an optical laser beam is applied collinearly, allowing the perfect overlapping of the optical laser and X-ray wave-packets both longitudinally and transversely. The dressing field of the optical laser would stimulate the X-ray pulse excited photo-electrons to absorb or emit a single or multiple optical laser photons, which is a simple quantum interpretation for the origin of the sideband features located at either the higher or the lower energy wing relative to the central photoemission peak (as in Fig. 5.20 (b), where only the higher energy sidebands are shown, and the lower energy sidebands which could be severely influenced by the retardation potential in the electron spectrometer are not shown). And the number of the sidebands as well as their relative intensities respected to the main peak could be used to indicate the level of the overlapping between the X-ray and optical laser wave-packets. If the beam transverse overlapping is optimized and well maintained (which is highly practical), then the sideband

intensity and fluctuation could only represent the overlapping of the two wave-packets in the longitudinal direction, i.e. the temporal delay and jitter of the X-ray/optical laser pulses.

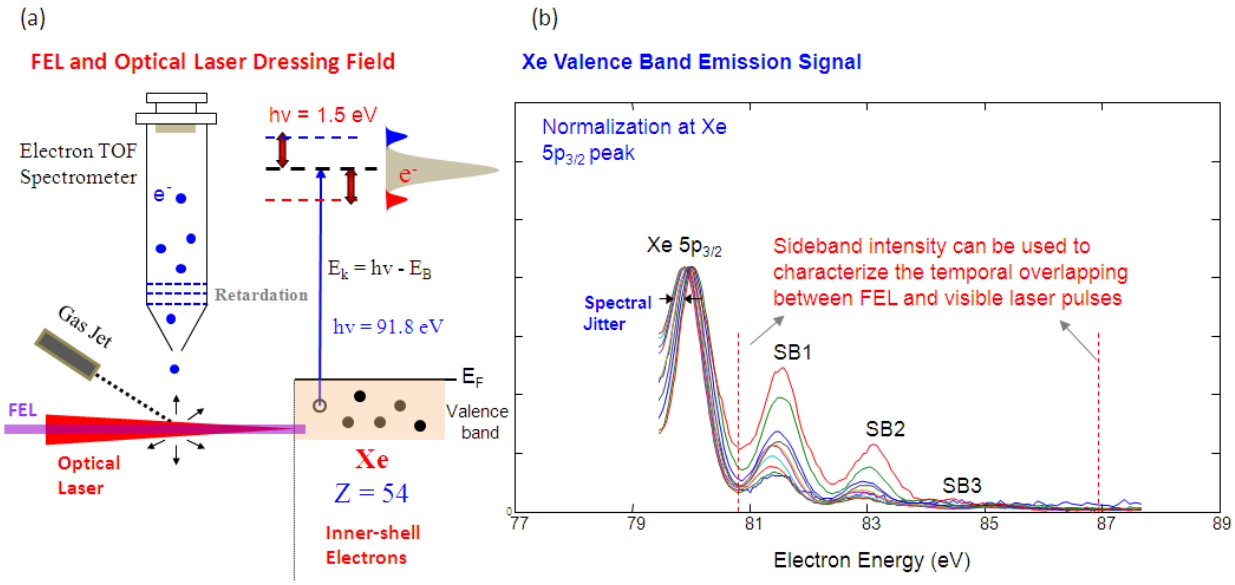

Fig. 5.20 *(a) The collinear layout of the X-ray FEL & Optical Laser beams is used for the two-color photoemission side-band measurement to characterize the temporal jitter of the X-ray/optical laser pulses. An electron TOF spectrometer is used to measure the photoemission from Xe valence band. (b) The sideband electron spectroscopy from Xe $5p_{3/2}$ peak, where the relative sideband intensity (normalized) could be used to monitor the overlapping in-between the X-ray/optical laser wave-packets (data from P. Radcliffe).*

A more generic sideband experiment was proposed and conducted in LCLS, where the technique is applied to the soft X-ray range with the photon energy of ~1keV, and the Auger electron spectroscopy instead of the primary electron emission is utilized [41]. The Auger process follows the inner-shell photo-ionization via filling the core-hole by an outer-shell electron, while the generated energy is immediately released as exciting an additional electron from the outer-shell (Fig.5.21 (a)). Therefore the Auger electron is an intrinsic process within the atom, associated with a constant and narrow spectral bandwidth, which won't be affected by the excitation X-ray photon energy and energy spread (or spectral width). And the KLL Auger electron of Ne atom would possess the kinetic energy of

$$E_k^{KLL} \approx E_{Binding}^{K(1s)} - E_{Binding}^{L(2p),0} - E_{Binding}^{L(2p),1st} \approx 804eV \quad (5.21).$$

Where the three items in the right side of the above equation are the electron binding energies of the K shell and the L(2p) shell in the ground (0) or the first excitation state (1st) respectively. Without the NIR laser dressing field applied, the Auger spectrum is measured as a sharp and narrow spectrum (mainly determined and limited by the electron spectrometer energy resolution); with the NIR laser is applied and overlapped with the X-ray beam, the photoemission spectrum would be significantly broadened, --- appearing as the sidebands. Especially when the temporal overlapping of the X-ray/NIR pulses is optimal, the central peak intensity is significantly depleted while the spectrum is broadened to maximal level, corresponding to the largest contribution from the sidebands (Fig.5.21 (b)).

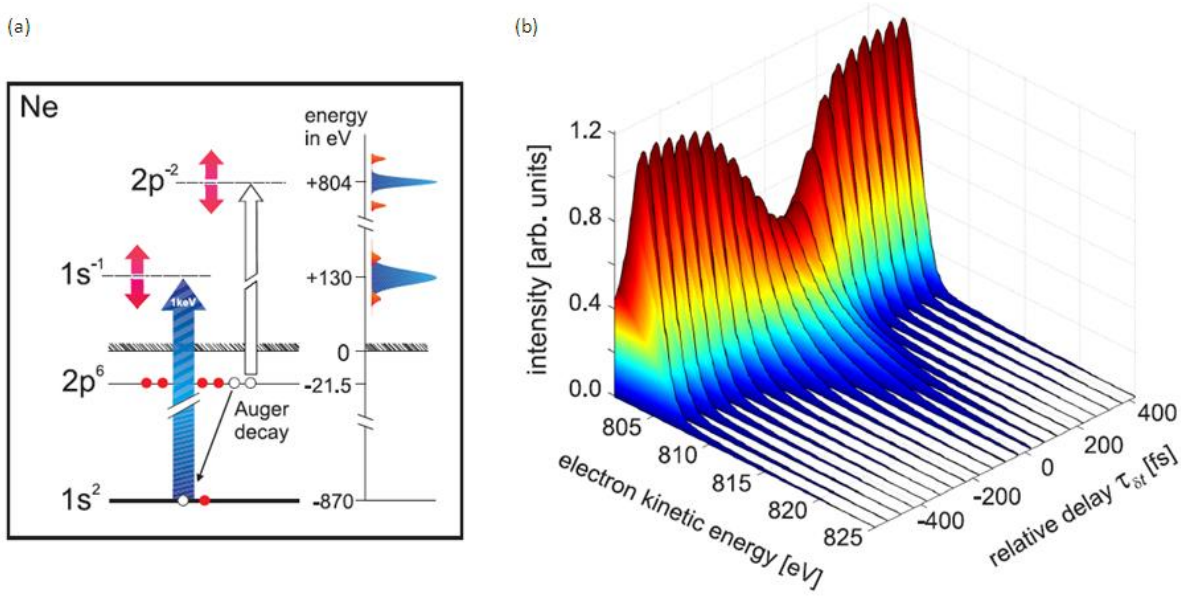

Fig. 5.21 *(a) the schematic energy diagram and the X-ray/optical laser two-color excitation schemes for the Ne atom, including both the 1s primary photon emission (at 130 eV) and the KLL Auger electron emission (at 804 eV) processes. (b) Ne Auger electron spectra (averaged) as a function of the setting delay time between the NIR laser and the X-ray pulses. The spectra near the relative zero-point is strongly depleted and broadened, indicating the maximal influence from the NIR laser dressing field (from [41]).*

If the classical formula discussed in the streaking technique (Section.5.12) is applied again,

$$W(\theta,t) = W_0 + 2U_p \cdot \sin^2(\varphi_i) \cdot \cos(2\theta) + \sqrt{8W_0U_p} \cdot \sin(\varphi_i) * \cos(\theta) \quad (5.22)$$

Where the relevant discussion in Section 5.12 is still valid, the Auger electron kinetic energy without the optical laser applied is $W_0 \approx E_k^{KLL}$, and the ponderomotive potential $U_p = e^2E_0^2(t)/4m_e\omega_L^2$ is calculated as ~0.07eV, providing the NIR laser wavelength and beam intensity are given by $\lambda_{NIR} \approx 0.8\,\mu m$ and $I_{NIR} \approx 1.2\times10^{12} Wcm^{-2}$ respectively. So the maximal energy change $\Delta W \approx 22eV$ is corresponding to the absorption (or emission) of 14 individual 1.55 eV NIR laser photons. In Fig.5.21 (b) only the spectral broadening not the individual sideband is observed, this is mainly because the energy resolution of the electron TOF spectrometer used in the experiment (~3 eV) is worse than the single optical laser photon energy (~1.55 eV), thus the individual sideband is not resolvable.

The Fig.5.21 (b) are associated with the averaged signals at each of the setting delays, where each spectrum is averaged by >1000 single-shot spectra to smooth the signal and enhance the S/N statistics. In order to develop and realize the X-ray pulse arrival monitor by using this technique, it would require the single shot measurement scheme as outlined in the Fig.5.22. The single short sideband intensity distribution of Ne photoemission in a short term experimental run is plotted in Fig.5.22 (a), each data point is generated through the integration of the normalized sideband region in a single-shot spectrum (e.g. the region in-between the two vertical dash lines in the Fig.5.20 (b)). Where 900 single shots are taken within 1-2 minutes, assuming the FEL is operated with a repetition of 10 Hz. Within such a short time scale, the slow electronic drift of the machine is minor, and the measured sideband intensity would approximately reflect the shot-by-shot temporal jitter for the X-ray pump-probe experiment. If the FWHM pulse durations for the X-ray and optical laser are 50 fs and 100 fs respectively and when the delay between the two pulses is larger than 300 fs (there is no temporal overlapping), so the sideband intensity is minimal (close to zero). On the other hand, the maximal sideband intensity is corresponding to the

time-delay zero. This is the base line of this technique. The temporal resolution of this method really depends on the accuracy to characterize the pulse shape and duration of both the X-ray and optical laser. Then the delay could be characterized as the sideband intensity. However the drawback is also obvious, since according to the principle for the sideband generation, it is impossible to differentiate for the same intensity whether the X-ray pulse arrives earlier or later respected to the optical laser pulse.

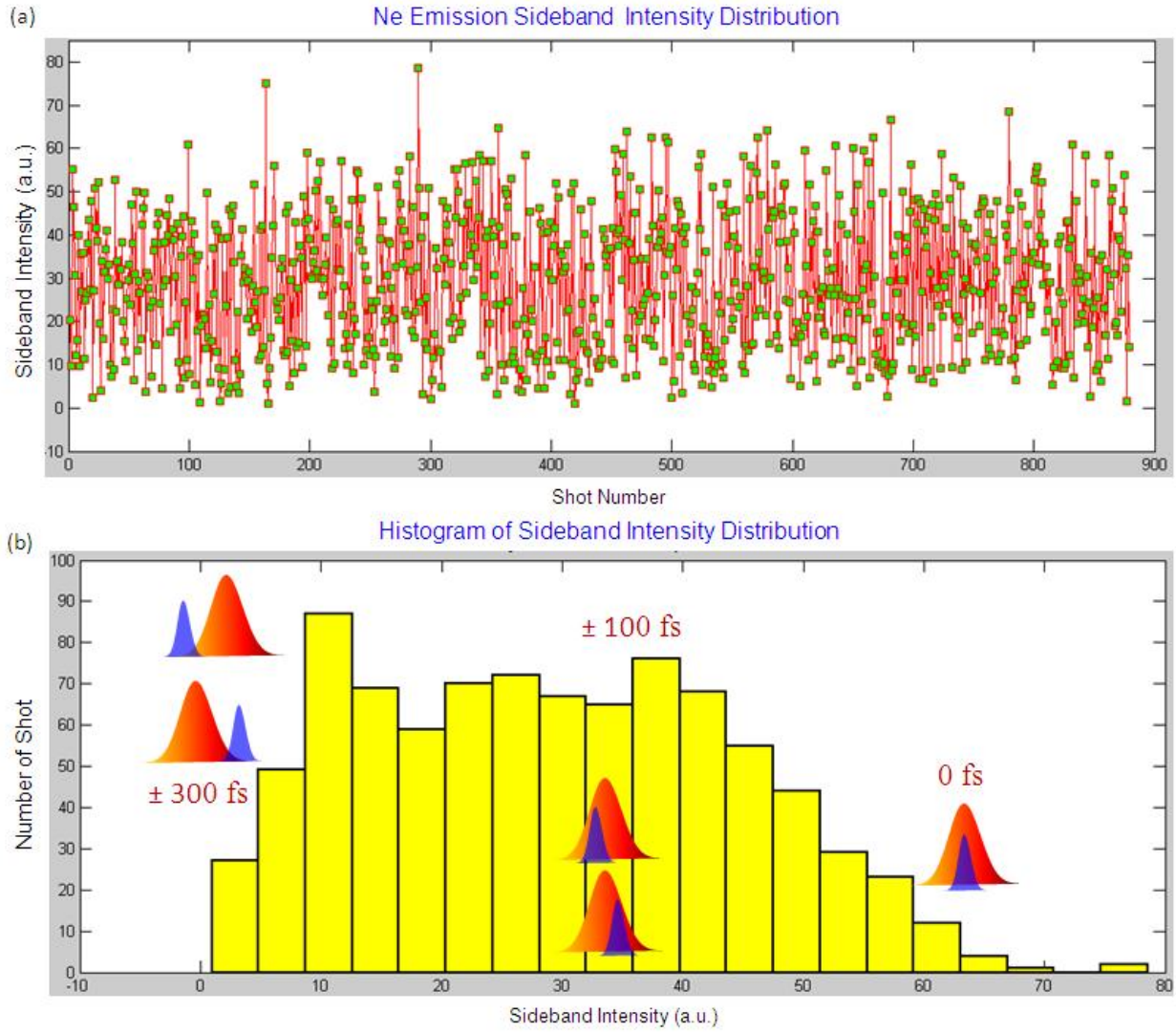

Fig. 5.22 *(a) The measurement and calibration of Ne photoemission sideband intensity for the Xray/optical laser single-shot experiment in a short term experimental run. (b) The histogram of the sideband intensity distribution for (a). And the inserted feature indicates the different levels of the overlapping between the X-ray pulse (blue, small) and the optical laser pulses (red, big), associated with the different sideband intensities (unpublished result).*

The gas-phase photoemission sideband spectroscopic technique has been developed and demonstrated working successfully in the XUV and soft X-ray range. Similar as the streaking method, this technique for the hard Xray is yet systematically investigated and not available. It might require applying the photoemission method to the high-Z gaseous atoms or the solid-state sample. Again since the electron energy spectrometer is the main tool for the technique, it would be essential to develop a high energy electron spectrometer (a few to 10 keV range) with high energy resolution down to sub-eV range, and with consistent and reliable performance. Moreover, the laser pulse providing the dressing field to the X-ray induced electron signals could be tuned up to carry linear-chirp, then the different temporal portions of the photo-emitted electrons (which map the temporary information of -Xray FEL pulses) interfere with different frequencies ω portions of the laser pulses, this would lead to broadening of sidebands and significant enhancement of sideband intensities, and apparently it is also the potential approach to differentiate at the same sideband intensity, the arrival times of X-ray/optical laser pulses (earlier or later). So this needs further theoretical and experimental work to clarify various conditions and circumstances.

6 Bibliography

[1] M. Altarelli, et al., The European X-ray Free Electron Laser Technical Design Report. 2006.

[2] Th. Tschentscher, Layout of the X-ray Systems at the European XFEL. 2011.

[3] E. A. Schneidmiller and M.V. Yurkov, Photon beam properties at the European XFEL. 2011.

[4] Z. Huang and K.-J. Kim, A Review of X-ray Free-Electron Laser Theory. 2006.

[5] M. Xie, Exact and Variational Solutions of 3D Eigenmodes in High Gain FELs. 2000.

[6] S. Reiche, et al., Start-to-end simulation for the LCLS X-ray FEL. Nucl. Instrum. Methods A, 2002. **483**: p. 70.

[7] S. Reiche, GENESIS 1.3: a fully 3D time-dependent FEL simulation code. Nucl. Instrum. Methods A, 1999. **429**: p. 243.

[8] W. Ackermann, et al., Operation of a free-electron laser from the extreme ultraviolet to the water window. Nature Photonics, 2007. **1**: p. 336.

[9] P. Emma, et al., First lasing and operation of an angstrom- wavelength free-electron laser. Nature Photonics, 2010. **4**: p. 641.

[10] C. Bressler, A. Galler, and W. Gawelda, FXE Conceptual Design Report. 2011.

[11] M. Meyer, SQS Scientific Instrument Conceptual Design Report. 2011.

[12] R. Mitzner, et al., Spatio - temproal coherence of free electron laser pulses in the soft x-ray regime. Optical Express, 2008. **16**: p. 19909.

[13] F. Sorgenfrei, et al., The extreme ultraviolet split and femtosecond delay unit at the plane grating monochromator beamline PG2 at FLASH. Review of Sci. Instr., 2010. **81**: p. 043107.

[14] M. Born and E. Wolf, Principles of Optics. 1999: Cambridge University Press.

[15] B. J. Thompson and E. Wolf, Two-Beam Interference with Partially Coherent Light. J. Opt. Soc. Am., 1957. **47**: p. 895.

[16] A. Singer, et al., Spatial and temporal coherence properties of single free-electron laser pulses. Optical Express, 2012. **20**: p. 17480.

[17] R. Mitzner and B. Siemer, Split and delay line for the XFEL. 2011, Westfaelische Wilhelms-University-Muenster

[18] Hamamatsu, Guide to Streak Cameras. 2012.

[19] H. Enquist, et al., Sub-picosecond hard x-ray streak camera using single-photon counting. Optics Letter, 2010. **35**: p. 3219.

[20] F. Krausz and M. Ivanov, Attosecond Physics. Review of Modern Physics, 2009. **81**: p. 163.

[21] U. Fruehling, et al., Single-shot terahertz-field-driven X-ray streak camera. Nature Photonics, 2009. **3**: p. 523.

[22] J. Itatani, et al., Attosecond Streak Camera. Physical Review Letter, 2002. **88**: p. 173903.

[23] A. L. Cavalieri, et al., Attosecond spectroscopy in condensed matter. Nature, 2007. **449**: p. 1029.

[24] A. Yariv, Quantum Electronics. 1988: John Wiley & Sons.

[25] A. L. Cavalieri, Simultaneous Measurement of X-ray Pulse Profile and Arrival Time at X-ray Free Electron Lasers. 2012: Hamburg.

[26] Y. Ding, et al., Ultra-short Electron Bunch and X-ray Temporal Diagnostics with an X-band Transverse Deflector. 2011.

[27] R. Akre, et al., Bunch Length Measurements using a Transverse RF Deflecting Structure in the SLAC LINAC, in EPAC. 2002: Paris, France

[28] S. Duesterer, et al., Spectroscopic characterization of vacuum ultraviolet free electron laser pulses. Optics Letter, 2006. **31**: p. 1750.

[29] C. Gahl, et al., A femtosecond X-ray/optical cross-correlator. Nature Photonics, 2008. **2**: p. 165.

[30] W. F. Schlotter, Determining Temporal Coincidence between the IR and X-ray Laser Pulses at LCLS. 2011, SLAC National Laboratory

[31] T. Maltezopoulos, et al., Single-shot timing measurement of extreme-ultraviolet free-electron laser pulses. New J. Physics, 2008. **10**: p. 03326.

[32] M. Drescher, et al., Time-diagnostics for improve dynamics experiments at XUV FELs. J. Phys. B: At. Mol. Opt. Phys., 2010. **43**: p. 194010.

[33] B. Li, et al., Preliminary Report for LCLS SXR L820 In-House Research Campaign 2012, European XFEL GmbH.

[34] M. Harmand, A reliable, easy-to-use timing tool for pump-probe experiments at X-ray FEL facilities 2012: Hamburg.

[35] M. Bionta, et al., Spectral encoding of X-ray/Optical Relative Delay. Optical Express, 2011. **19**: p. 21855.

[36] G. Geloni, et al., Theory of edge radiation - Part I: Foundations and basic applications. Nucl. Instrum. Methods A, 2009. **605**: p. 409.

[37] F. Tavella, et al., Few-femtosecond timing at fourth-generation X-ray light sources. Nature Photonics, 2011. **5**: p. 162.

[38] E. Hecht, Optics (4th Edition). 2002, New York: Addison Wesley.

[39] P. Radcliffe, et al., Single-shot characterization of independent femtosecond extreme ultraviolet free electron and infrared laser pulses Applied Physics Letters, 2007. **90**: p. 131108.

[40] M. Meyer, et al., Two-colour experiments in the gas phase. J. Phys. B: At. Mol. Opt. Phys., 2010. **43**: p. 194006.

[41] S. Duesterer, et al., Femtosecond x-ray pulse length characterization at the Linac Coherent Light Source free-electron-laser. New J. Physics, 2011. **11**: p. 093024.

[42] K. Oleg et. al., Thin film transient reflectivity measurement at SXR in-house research. 2011, SLAC National Laboratory

7 Acknowledgement

The author appreciates the kind support from J. Gruenert and S. Molodtsov to this work, and their comments for revision of the manuscript.

The author also thanks the invaluable discussion with W. F. Schlotter, O. Krupin, P. Radcliffe, M. Beye, Y. Li, G. Geloni, U. Frühling, R. Mitzner, A. L. Cavalieri, M. Bionta, R. Coffee, S. Duesterer, W. Wurth, M. Dell'Angela, F. Sorgenfrei, H. Redlin, T. Maltezopoulos, M. Wieland, G. Patrick, M. Felber, N. Kabachnik et. al.